

Boosting photocatalytic hydrogen production from water by photothermally induced biphasic systems

Shaohui Guo ¹, Xuanhua Li ¹, Ju Li ² & Bingqing Wei ³ 

Solar-driven hydrogen production from water using particulate photocatalysts is considered the most economical and effective approach to produce hydrogen fuel with little environmental concern. However, the efficiency of hydrogen production from water in particulate photocatalysis systems is still low. Here, we propose an efficient biphasic photocatalytic system composed of integrated photothermal-photocatalytic materials that use charred wood substrates to convert liquid water to water steam, simultaneously splitting hydrogen under light illumination without additional energy. The photothermal-photocatalytic system exhibits biphasic interfaces of photothermally-generated steam/photocatalyst/hydrogen, which significantly reduce the interface barrier and drastically lower the transport resistance of the hydrogen gas by nearly two orders of magnitude. In this work, an impressive hydrogen production rate up to $220.74 \mu\text{mol h}^{-1} \text{cm}^{-2}$ in the particulate photocatalytic systems has been achieved based on the wood/CoO system, demonstrating that the photothermal-photocatalytic biphasic system is cost-effective and greatly advantageous for practical applications.

¹State Key Laboratory of Solidification Processing, Center for Nano Energy Materials, School of Materials Science and Engineering, Northwestern Polytechnical University, Xi'an, China. ²Department of Nuclear Science and Engineering, Massachusetts Institute of Technology, Cambridge, MA, USA. ³Department of Mechanical Engineering, University of Delaware, Newark, DE, USA. email: lixh32@nwpu.edu.cn; weib@udel.edu

Solar-driven hydrogen production from water is a potentially efficient way to address the environmental problems and global energy crisis of fuel production. In particular, hydrogen gas has a high energy capacity (143 MJ kg^{-1}) and releases no toxic emissions¹. Therefore, an efficient and rapid photocatalytic hydrogen-production method is urgently needed^{2,3}. There are three main types of solar-driven hydrogen production systems: particulate photocatalysis, photovoltaic-assisted electrolysis (PV-E), and photoelectrochemical cells (PEC)², where the particulate photocatalysis is predicted to be more cost-effective than the other two systems⁴. Unfortunately, the solar to hydrogen conversion efficiency in particulate photocatalysis remains low though many strategies, including structural and defect engineering, plasmonic effects, and elemental doping, have been discussed to improve photocatalysts' optical absorption and photo-induced charge separation and transport^{5–7}.

In this work, from the phase-interface perspective, we design an efficient and cost-effective photocatalytic system composed of integrated photothermal–photocatalytic materials that can easily convert liquid water to water steam via photothermal transpiration effect with charred wood substrates. And the steam is simultaneously split into hydrogen by the photocatalysts loaded on the wood under light illumination without additional energy. The design exhibits biphasic interfaces of self-generated steam/photocatalyst loaded on the charred wood substrates/hydrogen gas. Our strategy of the photothermally induced biphasic interfacial feature differs from previous studies of the room-temperature vapor in moisture environment to reduce the catalysts corrosion (the humidity was realized through a complex microfluidic microreactor^{8–10}, convection effect¹¹, and hydrophobic effect¹²) and plasmonic thermal effects¹³ and near-infrared photothermal effects^{14,15} in the triphase interfaces of liquid water/photocatalyst/hydrogen. This photothermal–photocatalytic biphasic system kinetically lowers the hydrogen gas's transport resistance by nearly two orders of magnitude to allow the easy escape of hydrogen gas from the system. It also thermodynamically reduces the interface barrier in the adsorption process of gas-phase water molecules to photocatalysts. In this work, such a biphasic system significantly improves the photocatalytic hydrogen production rate up to $220.74 \mu\text{mol h}^{-1} \text{ cm}^{-2}$ for the wood/CoO system and $3271.49 \mu\text{mol h}^{-1} \text{ cm}^{-2}$ for the wood/CuS–MoS₂ hetero-photocatalyst.

Results

Constructing a photothermal–photocatalytic system on charred wood. A photothermal–photocatalytic system was skillfully designed and implemented by applying natural wood to generate water steam via photothermal transpiration under the light illumination simulated by a solar simulator at AM 1.5 G illumination (100 mW cm^{-2})^{16–18}. Also serving as the substrate for the photocatalytic reaction, a wood slice was cut from a tree perpendicular to its growth direction, and the surface of the wood slice was carbonized by a simple heating process for improving the steam generation with a high solar-to-steam-conversion efficiency of 46.90% (Fig. 1a and Supplementary Figs. 1–4)¹⁷. CoO nanoparticles (NPs), as a typical photocatalyst, were spin-coated on the carbonized wood slices to construct the wood/photocatalyst photothermal–photocatalytic system (here, the wood/CoO system), as shown in Fig. 1a. The monodispersed CoO NPs are $\sim 50 \pm 5 \text{ nm}$ in diameter, and the CoO lattice fringes (with a d-spacing of 0.24 nm) are assigned to the (111) lattice planes of CoO, as shown in Supplementary Fig. 5¹⁹. The light absorption peak of the CoO NPs locates at 550 nm (Supplementary Fig. 6).

The CoO NPs are distributed $\sim 2 \text{ mm}$ along the walls of the wood microchannels, as evidenced by the Raman spectra at different depths from the top surface (Fig. 1b), where only four

Raman spectra taken with an interval of $500 \mu\text{m}$ from the surface show the CoO Raman characteristic peaks at 473.6 and 540.9 cm^{-1} ²⁰. When the wood/CoO system floats in the water, the immersion depth of the wood in the water is about 2 mm (Fig. 1c), indicating that the photocatalysts are not directly soaked in the liquid-phase water.

After CoO NPs coating on the wood, the wood/CoO system shows high light absorbance from 300 to 1000 nm compared to that of the pure wood, as shown in Fig. 1d, implying that the wood/CoO system can effectively utilize solar energy. Under light illumination, the surface temperature of the wood/CoO system is about 325 K (Fig. 1e), and the adhered photocatalysts become covered with steam produced by the photothermal transpiration in the wood interior. Simultaneously, the photo-induced electrons participate in the hydrogen evolution reaction at the photocatalytic active sites, and photo-induced holes participate in the H₂O₂ generation (Fig. 1a). It should be noted that the local temperature of the CoO NP is estimated to be 346 K based on the potential (Fig. 1f, g, and Supplementary Fig. 7)²¹, which is higher than the global temperature (325 K, in Fig. 1e) because of the nanoscale effect. It is speculated that a higher local temperature is beneficial to enhance the photocatalytic reaction efficiency.

We investigated the effect of CoO NPs mass loading on the photocatalytic hydrogen gas production rate in the wood/CoO system (Fig. 2a). An optimized mass loading of about 38 mg cm^{-2} CoO NPs has been identified based on the experimental results. The photocatalytic H₂ evolution rate in the wood/CoO system with 38 mg cm^{-2} CoO NPs loading is about $5776 \mu\text{mol h}^{-1} \text{ g}^{-1}$ (i.e., $220.74 \mu\text{mol h}^{-1} \text{ cm}^{-2}$), 17 times higher than that of the triphase CoO NPs ($337 \mu\text{mol h}^{-1} \text{ g}^{-1}$, agrees well with the values reported under similar conditions)¹⁹, as shown in Fig. 2b. For clarification, the photocatalytic activity of wood alone was measured under the same condition (Supplementary Fig. 8), and no trace of hydrogen gas and oxygen gas were detected after 2 h of reaction, indicating that the wood does not have photocatalytic activity. Moreover, we also studied the effect of solar intensity on the photocatalytic response of the wood/CoO system. As shown in Fig. 2c, the rate of hydrogen evolution grows with the increase of solar intensity but not a linear relation. This is mainly because of the temperature rising on the wood/CoO surface caused by the increase in solar intensity (Supplementary Fig. 9). A higher temperature can exponentially improve the rate of hydrogen evolution, as evidenced in the following section.

In addition, the biphasic wood/CoO system exhibits superior stability in photocatalytic activity. The long-period photocatalytic hydrogen production measurement with the wood/CoO system was conducted for 5 days (Fig. 2d). On day 1, the initial hydrogen production rate in 1 h is $221.56 \mu\text{mol h}^{-1} \text{ cm}^{-2}$, and the average hydrogen production rate during 8 h reaction is $194.14 \mu\text{mol h}^{-1} \text{ cm}^{-2}$. On day 5, the average hydrogen production rate during 8 h reaction is $174.73 \mu\text{mol h}^{-1} \text{ cm}^{-2}$. Thus, after 5 days (40 h) test, the photocatalytic hydrogen evolution performance maintains about 90%, exhibiting that photocatalytic stability can be significantly improved through the wood/catalysts system compared to that in the previous work, which only holds 1 h of reaction²². We also studied the morphological stability of the wood/CoO system. After the photocatalytic reaction, the CoO NPs remain well attached to the wood matrix structure, further confirming the stability of the wood/CoO system (Fig. 2e, f, Supplementary Figs. 10 and 11). There is little difference in the reflection spectra and X-ray photoelectron spectroscopy (XPS) spectra of the wood/CoO system before and after the photocatalysis process (Supplementary Figs. 12 and 13). Besides, the inductively coupled plasma emission (ICP) and ultraviolet–visible (UV–Vis) spectra of the bulk water in the wood/CoO system after the photocatalytic reaction have been measured (Supplementary

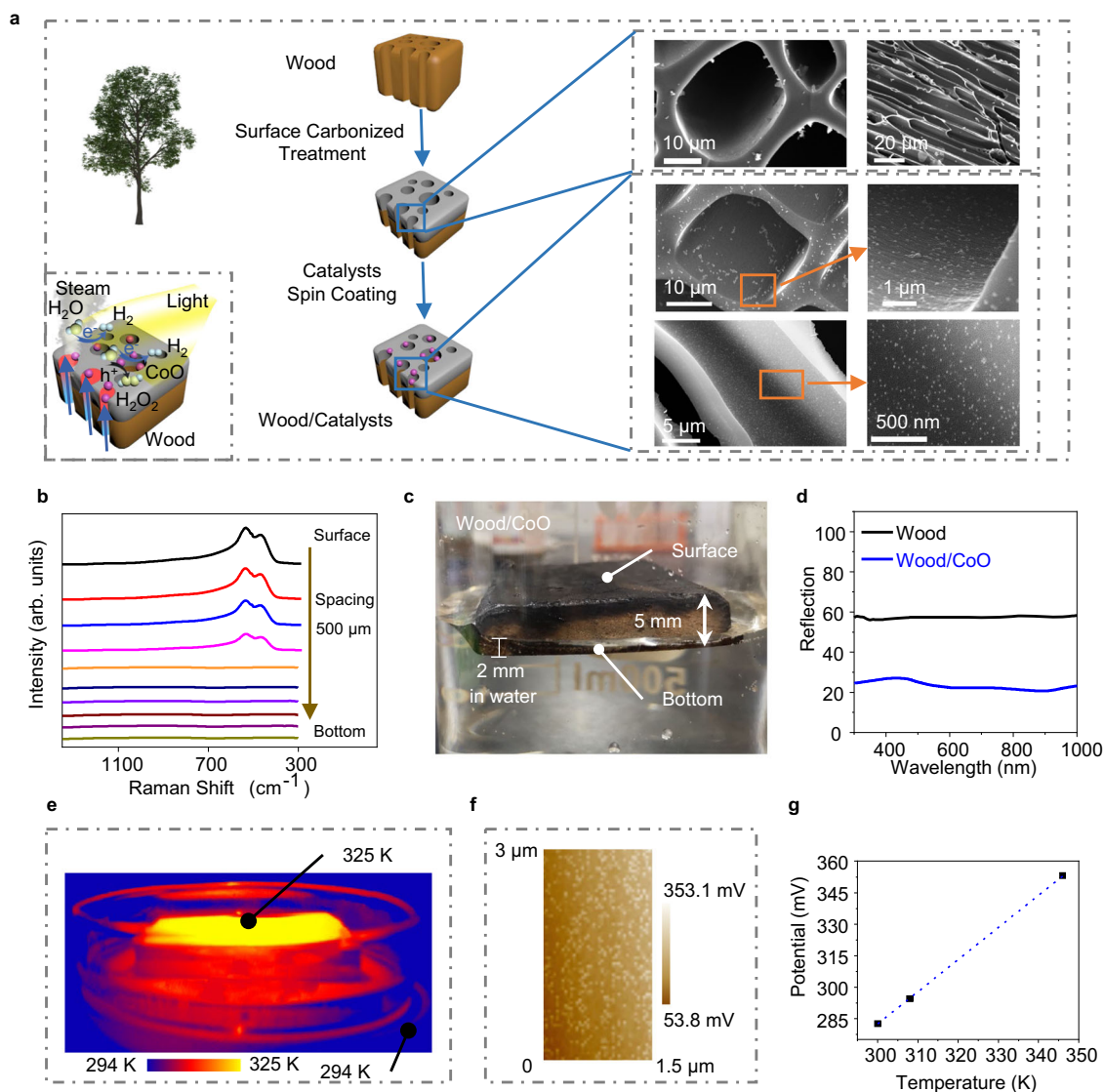


Fig. 1 The designed wood/photocatalyst biphasic photothermal-photocatalytic system. **a** Schematic of the fabrication process of the wood/photocatalyst structure that generates the water steam and catalyzes its splitting for hydrogen evolution. **b** Raman spectra taken at different depths along the cross-section of wood/CoO microchannels with an interval of 500 μm . **c** The photo of the wood/CoO system floating on water. **d** Reflection spectra of the wood and wood/CoO systems. **e** Infrared radiation thermal image from the wood/CoO system under light illumination. **f** The potential of wood/CoO under 100 mW cm^{-2} light illumination. **g** The estimated local temperature of CoO NPs through the measured potential.

Fig. 14 and Supplementary Table 1). There are few amounts of element Co in the bulk water based on the ICP measurement results and the absorption spectrum, exhibiting the wood/CoO system's excellent stability. It can be concluded that the photothermal-photocatalytic system displays a significant advantage in substantially enhancing the H_2 evolution rate from water splitting. It is noticed that the ratio of photocatalytic H_2 and O_2 production is not equal to 2:1 (Supplementary Figs. 15 and 16), mainly due to the generation of H_2O_2 by-product in the photocatalytic process (Supplementary Fig. 17).

Understanding the phase-interface effect on catalytic performance. From the phase-interface perspective, the photothermal-photocatalytic system exhibits biphasic interfaces of photothermally-generated steam/photocatalyst/hydrogen gas. To understand the phase-interface effect on the photocatalytic performance, we conducted experiments with a biphasic photocatalytic system containing injected water steam/solid photocatalysts (Fig. 3a and c). Water steam was injected and controlled by a steam flowmeter into

a transparent reactor, where CoO NPs powder catalysts were placed on the surface of a filter paper, and no sacrificial agent was added to the photocatalytic system. Under light illumination, the steam in the reactor was photocatalytically converted to H_2 , which was detected by the gas chromatography (GC) (Fig. 3c). For comparison, the liquid/solid/gas triphase system of water/photocatalyst/hydrogen in common photocatalytic hydrogen evolution reaction has also been included. As shown in Fig. 3b, hydrogen bubbles are generated when the solid photocatalysts are interacting with liquid water under light illumination. The produced hydrogen gas is then collected by passive transport against the liquid water phase.

Hydrogen production in the biphasic photocatalytic reaction system was evaluated with different flow rates of water steam (from 5 to 88 ml h^{-1}) injected into the reactor chamber (Fig. 3c, d, Supplementary Figs. 18 and 19). The rate of hydrogen production from steam increases along with the increase of steam flow rate from 5 to 62 ml h^{-1} . When the steam flow rate further grows, the hydrogen production rate is stabilized because the quantity of

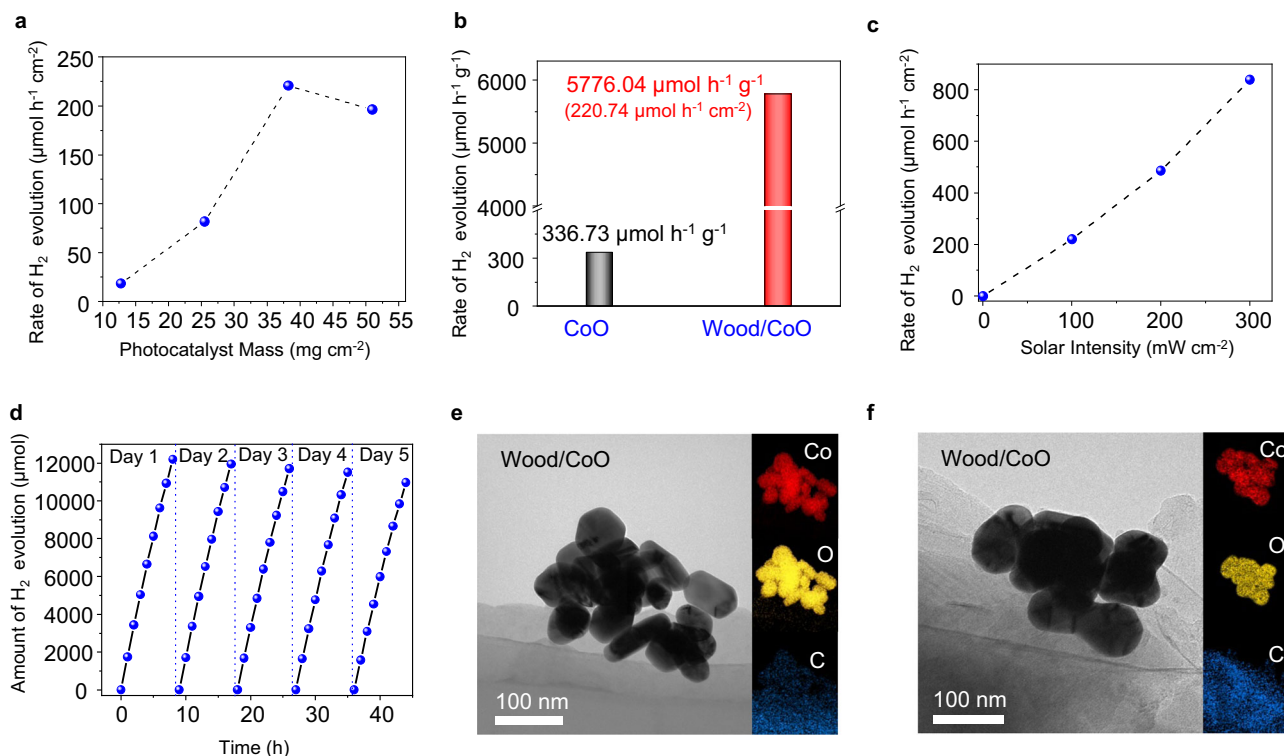


Fig. 2 Photocatalytic hydrogen evolution in the designed wood/photocatalyst biphasic photothermal-photocatalytic system. **a** Mass loading-dependent photocatalytic hydrogen gas production rates for the wood/CoO system (area: 7.85 cm²). **b** Rate comparison of H₂ evolution in the triphase CoO NPs system and wood/CoO biphasic photothermal-photocatalytic system (area: 7.85 cm², mass: 0.3 g). **c** Rate of H₂ evolution versus solar intensity from the wood/CoO system (area: 7.85 cm², mass: 0.3 g). **d** Time-dependent photocatalytic hydrogen gas production of the wood/CoO system for 5 days. The light source is a solar simulator at AM 1.5 G illumination (100 mW cm⁻²). **e** TEM images and EDS element mapping of CoO NPs attached to the walls of the wood microchannels before the photocatalytic reaction. **f** TEM images and EDS element mapping of CoO NPs attached to the walls of the wood microchannels after the photocatalytic reaction.

water molecules reaches saturation during the photocatalytic reaction. At the optimal flow rate (i.e., 62 ml h⁻¹), the maximum hydrogen evolution rate is ~6200 μmol h⁻¹ g⁻¹, 18 times higher than that in the triphase reaction system (337 μmol h⁻¹ g⁻¹). The biphasic photocatalytic system also shows excellent stability of the photocatalytic reaction, as shown in Fig. 3e. After three cyclic measurements, the amount of H₂ evolution concurs with that in the first measurement. And the morphology and absorption spectra of CoO NPs after the photocatalytic reaction also keep unchanged, confirming the excellent stability of the photocatalyst (Supplementary Figs. 5, 20, and Fig. 3f).

The main factors governing the photocatalytic hydrogen evolution in the biphasic reaction system are the temperature and the state of water in comparison to the triphase reaction system. Figure 4a shows the temperature-dependent of the photocatalytic hydrogen evolution rate with the CoO NPs photocatalyst in the triphase reaction system. As the reaction temperature increases from 298 K to close to 373 K, the hydrogen evolution rate monotonically increases from 336.73 to 1968.9 μmol h⁻¹ g⁻¹ (note that 373 K is the steam-conversion temperature of liquid water). It should be noted, however, no trace hydrogen is detected after 2 h of reaction at near 373 K if light illumination is not applied, implying that the catalytic reaction cannot be thermally triggered (Supplementary Fig. 21). Furthermore, the relationship between the rate of H₂ evolution reaction V and the reaction temperature T can be well-fitted with the Arrhenius equation:

$$V = 3748519.38e^{-\left(\frac{23023}{8.314T}\right)} \quad (1)$$

According to Eq. (1), the activation energy for the hydrogen production over CoO was deduced to be 23.023 kJ mol⁻¹. The activation energy is a key indicator to reflect whether photocatalytic hydrogen evolution reaction occurs easily. The smaller the activation energy is, the easier the hydrogen production process will become. Therefore, a low activation energy here indicates that the hydrogen production process is easily conducted on the CoO NPs. Furthermore, the H₂ evolution rate at 373 K is estimated to be 2236.76 μmol h⁻¹ g⁻¹. However, it is much lower than the H₂ evolution rate (6200.42 μmol h⁻¹ g⁻¹, see Fig. 3d) in the biphasic reaction system at the same temperature of 373 K, indicating that the temperature effect on improving the H₂ evolution rate is limited although a higher reaction temperature does promote the photocatalytic hydrogen-evolution reaction. Thus, in addition to the reaction temperature, the state of water plays a crucial role in enhancing the hydrogen evolution of the biphasic reaction system.

The temperature effect can be systematically analyzed from two aspects: thermodynamics and kinetics. Three reaction steps, including the adsorption of water molecules, the adsorption of hydrogen atoms, and the hydrogen gas production in photocatalytic reaction, have been involved. First, the Gibbs energy in the triphase system has been calculated at 298 and 373 K, where the pure CoO structure without any group is used to simulate the CoO status in the neutral environment because the pH value of the reactant water is approximately equal to 7. As shown in Fig. 4b, the change of reaction temperature from 298 K to 373 K influences the first and second steps. The Gibbs energy of the water molecule adsorption process at 298 K is about 0.426 eV, and it is about 0.145 eV for the hydrogen adsorption process.

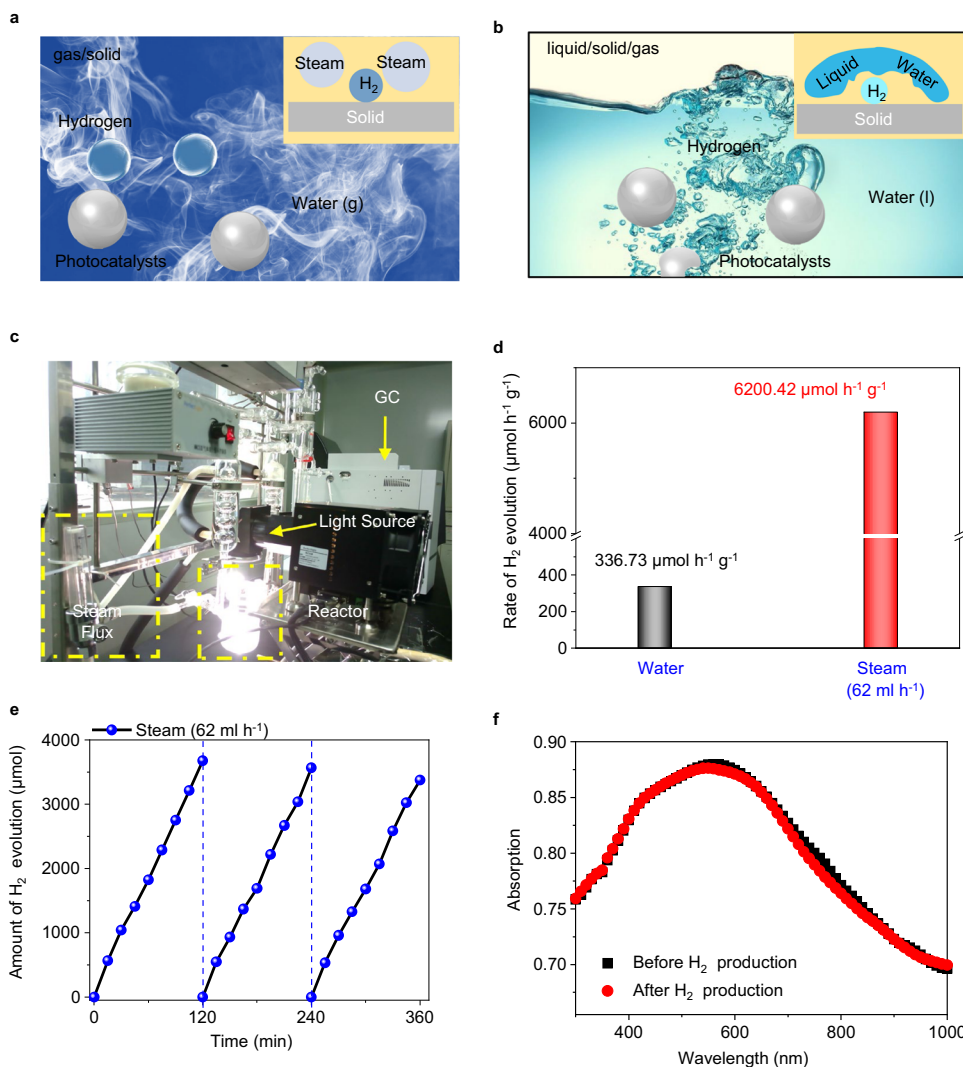


Fig. 3 Schematic and photocatalytic hydrogen evolution performance in the biphasic and triphasic reaction systems. **a** Schematic of the biphasic system with water steam/solid photocatalysts/hydrogen gas. **b** Schematic of a typical triphasic system consisting of liquid water/solid photocatalysts/hydrogen gas. **c** Photo of the biphasic photocatalytic system. **d** Photocatalytic hydrogen gas production rate from the triphasic and biphasic reaction systems. **e** Time-dependent photocatalytic hydrogen gas production from water steam with a flow rate of 62 ml h⁻¹. The light source is a solar simulator at AM 1.5 G illumination (100 mW cm⁻²). **f** The absorption spectra of CoO NPs before and after hydrogen gas production.

Comparatively, they are reduced to 0.331 and -0.054 eV, respectively, at 373 K. As expected, the high reaction temperature in the triphasic photocatalytic system would thermodynamically favor the water molecule adsorption process.

In addition to kinetically promote the transport of water molecules, high temperatures will reduce hydrogen transport resistance as well so that the photocatalytic reaction rate can be accelerated. This can be evidenced by the hydrogen gas diffusion coefficient D_L in a liquid-phase environment, calculated by the Stokes-Einstein equation:

$$D_L = 7.4 \times 10^{-8} \frac{T(\psi_{H_2O} M_{H_2O})^{0.5}}{\mu V_{H_2}^{0.6}} \quad (2)$$

where T is the temperature, ψ_{H_2O} (=2.26) is the “association” parameter of the solvent water, M_{H_2O} and μ denote the molecular weight and viscosity of water, respectively, and V_{H_2} is the molar volume of hydrogen. When the temperature is increased from 298 to 373 K, the hydrogen gas diffusion coefficient D_L is increased. Thus, hydrogen transport resistance is slightly decreased.

A more significant effect on promoting the photocatalytic hydrogen-evolution reaction comes from the state change of the water phase. When the water phase changes from liquid to steam at the same temperature (373 K), interestingly, the first and second step of the photocatalytic reaction (i.e., the water molecule adsorption process and the hydrogen adsorption process) has been significantly influenced. The Gibbs energy of the water molecule adsorption process substantially decreases from 0.331 eV in the triphasic system to -0.212 eV in the biphasic system, and it also reduces (-0.054 vs. -0.007 eV) for the hydrogen adsorption process (Fig. 4c), indicating that the water molecule adsorption process and hydrogen adsorption process in the biphasic system become much more comfortable than that in the triphasic system. Kinetically, the hydrogen gas diffusion coefficient D_G in the gaseous environment can be calculated by the Chapman-Enskog theory:

$$D_G = \frac{A * T^{3/2} \sqrt{\frac{1}{M_{H_2}} + \frac{1}{M_{H_2O}}}}{P * \sigma^2 * \Omega} \quad (3)$$

where A (=1.858 × 10⁻³) is an empirical coefficient^{23,24}, M is the

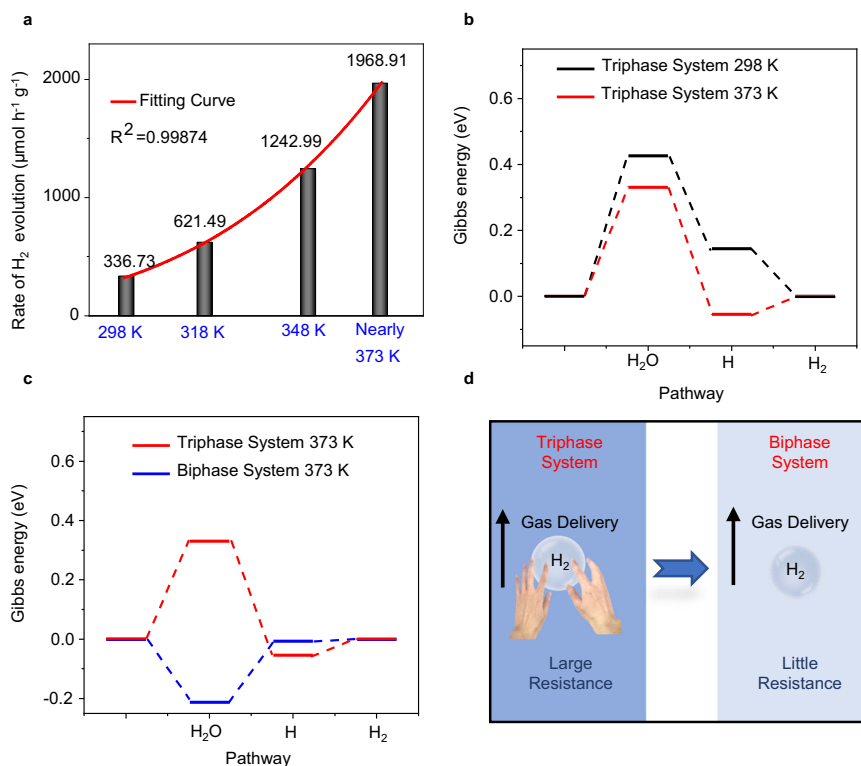


Fig. 4 The factors governing the biphasic photocatalytic hydrogen evolution: temperature and liquid-to-gas-phase changes of water. **a** The photocatalytic hydrogen evolution rate with the CoO NPs versus the reaction temperature in the triphase reaction system. (Here, the background pressure was maintained at 5 kPa). **b** Gibbs energy of a photocatalytic reaction in the triphase system with different temperatures over the pure CoO surface. The photocatalyst is CoO NPs. **c** Gibbs energy of a photocatalytic reaction in the triphase system (373 K) in comparison with the biphasic system (373 K) over the pure CoO surface. The photocatalyst is CoO NPs. **d** Schematic of the hydrogen transport resistances in the liquid- and gas-phase environments.

molar mass, P is the pressure in the system, σ is the average collision diameter, and Ω is a temperature-dependent collision integral. The produced hydrogen bubbles experience frictional resistance in adjacent interlayers from relative motion with the environmental particles²⁵. Owing to the interfacial frictional resistance, the hydrogen-gas diffusion coefficients differ significantly in the liquid and steam water phases. In the liquid water phase, D_L is $(4.99\text{--}5.06) \times 10^{-5}$ at reaction temperatures near 373 K (i.e., 368–373 K), based on the Stokes–Einstein equation (Eq. (2)), whereas, in the steam phase, D_G is 2.65×10^{-3} at 373 K, two orders of magnitude higher than that in the liquid water. Therefore, when the produced hydrogen gas passes through the liquid water before being liberated, it is greatly resisted by the environmental liquid water molecules. By contrast, the hydrogen bubbles in the biphasic system pass through the gas water molecules with much less resistance. Figure 4d schematizes the hydrogen transport resistances in the liquid- and gas-phase environments.

The universality of the photothermal–photocatalytic system.

In addition to the exemplary wood/CoO system, the photothermal–photocatalytic system can also extend to other photocatalysts. To demonstrate the universal feature of the photothermal–photocatalytic biphasic system, different photocatalysts, i.e., MoS₂, C₃N₄, and TiO₂ were, respectively, spin-coated on the carbonized wood slices to construct wood/photocatalyst architectures (Fig. 5a–c and Supplementary Figs. 22–24). The MoS₂, C₃N₄, and TiO₂ photocatalysts are all uniformly distributed and attached to the microchannel walls of the wood. The particulate photocatalytic hydrogen-evolution reactions were carried out in all the wood/photocatalyst reaction systems (Fig. 5d and Supplementary Fig. 25).

All of the photocatalysts realize photothermal–photocatalytic hydrogen production, but no oxygen is detected at the same time because of the difficulty in downshifting the valence band positions (e.g., MoS₂, C₃N₄) and complex surface deformation reaction (e.g., TiO₂)^{26–28}. The H₂ average production rates of the wood/MoS₂, wood/C₃N₄, and wood/TiO₂ photothermal–photocatalytic systems are 155.77, 95.54, and 59.87 μmol h⁻¹ cm⁻², respectively. For each photocatalyst, the apparent quantum yield (AQY) of the photothermal–photocatalytic biphasic system dominates compared with the previously reported photocatalyst systems (Fig. 5e)^{29–41}, and the measured data are listed in Supplementary Table 2.

In addition to the monothetic particulate photocatalysts, a heterojunction photocatalyst, i.e., CuS–MoS₂, has also been introduced to the photothermal–photocatalytic systems to verify the universality (Supplementary Fig. 26). Similar to the monothetic particulate photocatalysts, the CuS–MoS₂ photocatalyst has adhered to the microchannel walls of the wood matrix, as shown in Fig. 5f. The photocatalytic H₂ average production rate of the biphasic wood/CuS–MoS₂ photothermal–photocatalytic system reaches up to 85,604 μmol h⁻¹ g⁻¹ (Supplementary Fig. 27), 16 times that of the triphase CuS–MoS₂ photocatalyst (5350 μmol h⁻¹ g⁻¹) (Supplementary Fig. 28). It is noted that no photocatalytic oxygen gas was produced because of the energy band positions of the CuS–MoS₂ photocatalyst (Supplementary Fig. 29)⁴². It is speculated that the photo-induced holes react with some S ions from CuS/MoS₂ catalyst as shown based on the XPS results (Supplementary Fig. 30)⁴³. Figure 5g summarizes the H₂ evolution rates of typical particulate photocatalysts reported to date. The H₂ evolution rates were 70,000, 64,426, and 11,090 μmol h⁻¹ g⁻¹ in InP/ZnS⁴⁴, PTB7-Th/EH-IDTBR NPs⁴⁵, and 2D/2D NiS/Vs-ZnIn₂S₄/WO₃⁴⁶, respectively. They were 23,410 and 16,300 μmol h⁻¹ g⁻¹ based on the

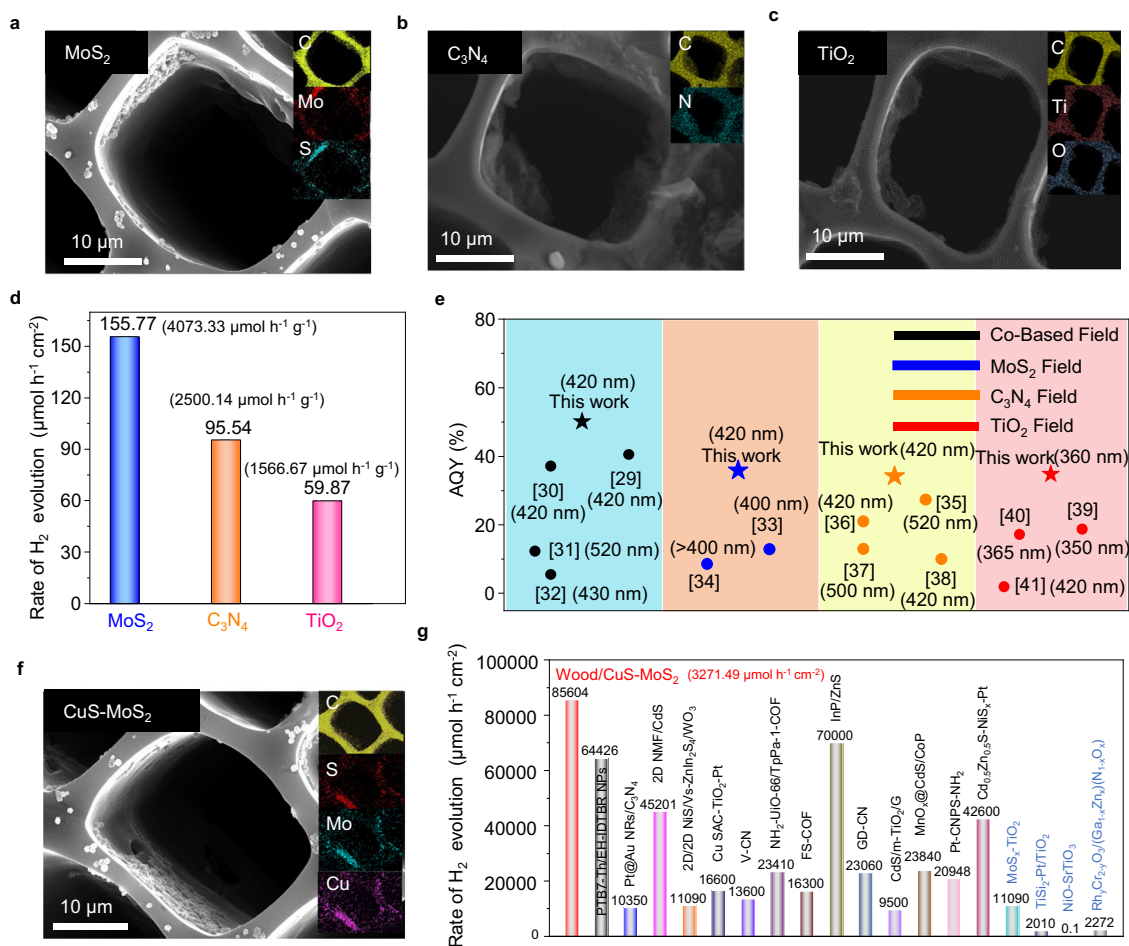


Fig. 5 The universal feature of the photothermal-photocatalytic biphasic system for photocatalytic hydrogen evolution from water. **a** SEM images and EDS mapping of the wood/MoS₂. **b** SEM images and EDS mapping of the wood/C₃N₄. **c** SEM images and EDS mapping of the wood/TiO₂ systems. **d** H₂ evolution rates of the wood/MoS₂, wood/C₃N₄, and wood/TiO₂ systems. **e** Comparison of the AQY with literature in different particulate photocatalytic systems of TiO₂, C₃N₄, MoS₂, and Co-based photocatalysts, respectively. The numbers are the reference numbers and light wavelength. The maximum AQY data in literature and measurement results are presented for comparison. **f** SEM image and EDS mappings of the wood/CuS-MoS₂ photothermal-photocatalytic system. **g** Comparison of the H₂ evolution rate of different particulate photocatalytic systems reported to date. The blue fonts on the right represent the photocatalytic reaction in the gas-phase water environment. The light source is a solar simulator at AM 1.5 G illumination (100 mW cm⁻²).

COF materials^{47,48}. The CdS-based photocatalysts including 2D NMF/CdS⁴⁹, Cd_{0.5}Zn_{0.5}S-NiS_x-Pt⁷, MnO_x@CdS/CoP⁵⁰, and CdS/m-TiO₂/G⁵¹ achieved a H₂ evolution rate of 45,201, 42,600, 23,840, and 9500 μmol h⁻¹ g⁻¹, respectively. An H₂ evolution rate of 16,600 μmol h⁻¹ g⁻¹ was reported on the Cu SAC-TiO₂-Pt photocatalyst⁵². The optimized C₃N₄-based heterojunction photocatalysts, including GD-CN⁵³, Pt-CNPS-NH₂⁵⁴, V-CN⁵⁵, and Pt@Au NRs/C₃N₄⁵⁶ achieved an H₂ evolution rate of 23,060, 20,948, 13,600, and 10,350 μmol h⁻¹ g⁻¹, respectively. In the reports involving vapor phase water, the photocatalytic hydrogen production rates were relatively low^{12,57,58}, and the leader was 11,090 μmol h⁻¹ g⁻¹ based on the MoS_x-TiO₂ hybrid¹¹. The photothermal-photocatalytic system, i.e., the wood/CuS-MoS₂ device, outperforms all of these photocatalysts with an H₂ evolution rate of 85,604 μmol h⁻¹ g⁻¹ (i.e., 3271.49 μmol h⁻¹ cm⁻²) without any external assistance, e.g., sacrificial agents, photovoltaic or photoelectrochemical assistance, demonstrating that the photothermal-photocatalytic biphasic system can substantially enhance the photocatalytic hydrogen evolution from water.

Moreover, the photothermal-photocatalytic biphasic system is promising for practical applications because it can easily be realized through the transpiration process of wood loaded with

particulate photocatalysts. This natural process converts liquid water to steam under the same light illumination without additional energy input. As an example of a demonstration, the wood/CuS-MoS₂ was put in a reaction cell filled with simulated seawater (Supplementary Fig. 31), and the hydrogen collector was connected to the gas outlet. When exposed to natural sunlight, the hydrogen collector exhibits a visible bulge after 2 h of reaction. Although the salts (e.g., NaCl) in the seawater are possible to adhere to wood tunnels to clog the matrix structures, which lead to a decrease in steam production during evaporation⁵⁹, the H₂ production rate in this exemplary test is about 37,219 μmol h⁻¹ g⁻¹ (i.e., 1422.38 μmol h⁻¹ cm⁻²) (measured by GC), confirming the strong photocatalytic ability in a seawater environment. And after 6 h of reaction, the H₂ production rate remains consistent with that from the first test, exhibiting excellent photocatalytic stability.

Discussion

We have designed and demonstrated an integrated photothermal-photocatalytic system that helps achieve the dominant photocatalytic hydrogen evolution rate of 85,604 μmol h⁻¹ g⁻¹ (i.e., 3271.49 μmol h⁻¹ cm⁻²) among the particulate photocatalysts.

Such excellent performance was achieved by replacing the traditional triphase photocatalytic interfaces (liquid water/photocatalyst solid/hydrogen gas) with the biphasic photocatalytic interfaces (photothermally-generated water steam/photocatalysts loaded on charred wood substrates/hydrogen gas). The wood carrier functions simultaneously as the photocatalyst substrate as well as the steam generator under solar light, which is significantly advantageous for practical applications. This photothermal-photocatalytic system reduced the barrier of the water molecule adsorption process and minimized the delivery resistance of the produced hydrogen gas, enabling efficient and environmentally safe fuel for next-generation applications on an industrial scale.

Methods

Synthesis of CoO, MoS₂, C₃N₄, TiO₂, and CuS-MoS₂ photocatalysts. CoO NPs were fabricated by a heating process with the hydrothermal method and a tube furnace. In all, 2 g of Co(CH₃COO)₂·4H₂O powder was added to a mixed solvent with 8 ml n-octanol and 32 ml ethanol by stirring for 3 h. After that, the mixture was transferred to a 50 ml Teflon-lined stainless steel autoclave, and then heated at 200 °C for 6 h. When the autoclave was cooled down to room temperature, the powders were placed in a quartz tube furnace. The tube was filled to ambient pressure with Ar gas flowing at 240 s.c.c.m. The Ar flow rate and 1 atm. pressure were maintained throughout the preparation process. The tube was continuously heated from 25 °C to 600 °C in 3 h. After maintaining the tube furnace at 600 °C for 5 h, the tube was cooled to room temperature over 5 h. The obtained powders were then dispersed in pure water, and the CoO NPs were obtained by centrifugation at 1677 × g for 10 min (Anke TGL-15B Centrifuger). After that, the prepared photocatalysts (0.3 g) were added to the surface of the filter paper by spin coating at 500 rpm for 20 s. Then the filter paper with photocatalyst was taken into the oven at 40 °C for 1 h.

For the MoS₂ synthesis, solutions of 2.0 mmol Na₂MoO₄ and 4.0 mmol L-cysteine were sterilized in a 50 ml Teflon-lined stainless steel autoclave. The autoclave was heated at 200 °C for 12 h and naturally cooled to room temperature, obtaining the MoS₂ solution. For the C₃N₄ synthesis, 0.5 g C₃N₄ powder was exfoliated in deionized water (400 ml) for 8 h with a probe ultrasonication cleaner (200 W, UP400S). The dispersion was then centrifuged at 2029 × g for 20 min, yielding the C₃N₄ photocatalyst. TiO₂ was synthesized by the nonhydrolytic sol-gel approach described as follows. A solution of TiCl₄ (1 ml), ethanol (5 ml), and benzyl alcohol (35 ml) was incubated for 6 h at 80 °C, then washed three times with diethyl ether. After centrifuging the crude product at 2415 × g for 10 min, a white TiO₂ precipitate was obtained. The final TiO₂ solution was prepared by dispersing the precipitate in ethanol.

For the CuS-MoS₂ synthesis, the process was divided into two steps. A Cu-Mo-based metal-organic framework (i.e., NENU-5) was first prepared through a wet chemical method. 0.6 g copper (II) acetate monohydrate and 1.2 g phosphomolybdic acid hydrate were mixed and sonicated in 40 mL DI water for 30 min. 0.62 g trimeric acid, which was dissolved in 40 ml ethanol, was poured into the above solution quickly, and the nanocrystal NENU-5 was obtained. Second, 2 g sulfur powder and 0.1 g NENU-5 were placed in a dual-zone tube furnace up-stream region (250 °C) and down-stream region (550 °C), respectively. The CuS-MoS₂ heterojunction was prepared after 1 h reaction under Ar gas environment.

Synthesis of wood/photocatalyst systems. Pinewood blocks were cut into pieces using a sweep saw (area: 7.85 cm², thickness: 5 mm). The whole carbonized wood was directly obtained through heating the woodblock in a muffle furnace at a temperature of 300 °C for 2 h. To improve the steam generation, the surface of the wood slice was treated by a simple heating process to obtain the surface carbonized wood. In detail, the wood samples were pretreated in an alcohol flame for 2 min, then immediately immersed in cold water at room temperature for rapid quenching. Next, the NP solutions (0.3 g of CoO, MoS₂, C₃N₄, TiO₂, or CuS-MoS₂) were spin-coated onto the wood surface at 500 rpm for 20 s. Finally, the samples were dried in an oven at 45 °C for 2 h, yielding the wood/catalyst systems. The different CoO loadings (0.1, 0.2, 0.3, and 0.4 g) were realized by changing the photocatalyst solution concentration.

Characterization of the photocatalysts. The morphologies of the samples were characterized by a scanning electron microscope (SEM) (FEI NOVASEM) and a transmission electron microscope (TEM) (FEI Talos F200X). The infrared radiation thermal image from the wood/CoO system under light illumination was recorded with a UTi80 thermal imager. XPS spectra of wood/CoO and element S for CuS/MoS₂ were collected through Kratos Axis supra XPS spectrometer. The local temperature of CoO NPs was estimated through the atomic force microscopy (AFM) (Bruker Dimension Icon). At the 300 and 308 K, the potentials of wood/CoO were measured. After that, the potential of wood/CoO was recorded under

100 mW cm⁻² light illumination. Due to the correlation between potential and the temperature²¹, the local temperature of CoO under light illumination could be estimated. The bulk water of wood/CoO was measured through Perkin Elmer Lambda 35 ultraviolet-visible spectrophotometer and Thermo Fisher ICAP7600-DUO inductively coupled plasma emission spectrometer.

Solar-driven-steam generation measurements. Steam generation from the wood was measured in a quartz beaker containing deionized (DI) water. The solar light was simulated by a solar simulator at AM 1.5 G illumination (100 mW cm⁻²), and the mass changes in the water were measured by a high-accuracy balance (Mettler-Toledo, ME204E). The quartz beaker containing the wood in DI water was placed on the balance, and the weight loss of the water was recorded by reading the balance every 3 min under light illumination.

The solar-to-steam-conversion efficiency η was calculated as:

$$\eta = \frac{\Delta m * \Delta v_{ap} * H}{M * P * S * T} \quad (4)$$

where Δm is the mass loss of water during irradiation, $\Delta v_{ap} * H$ is the phase change enthalpy of water from liquid to vapor which is $-40.637 \text{ kJ mol}^{-1}$, M is the molar mass of water, P is the solar power density (100 mW cm⁻²), S is the area (about 7.85 cm²), and T is the irradiation time (3600 s).

Hydrogen generation tests. For the hydrogen evolution measurement in the liquid water/photocatalysts/hydrogen-gas triphase system, 50 ml of deionized water was added to the transparent reactor chamber, and then the filter paper with photocatalyst was immersed in the water. The reaction cell was placed 7.0 cm from the light source. The light source was a solar simulator at AM 1.5 G illumination (100 mW cm⁻²) (CEL-NP2000) (Supplementary Fig. 32), which was equipped with a fan that efficiently dissipated the excess heat. The reaction temperature in the quartz cell was tuned through a heating jacket and was measured by a thermometer. During the photocatalytic reaction, the gases were transferred into the sample loop by a peristaltic pump and were further quantified by gas chromatography (Shimadzu GC-2014c; Ar carrier gas and molecular sieve-5A column), equipped with a thermal conductivity detector. The hydrogen-gas yield of the reactor was measured every 15 min.

The hydrogen evolution in the injected water steam/photocatalysts biphasic system was carried out similarly to the triphase reaction measurement. The filter paper with photocatalysts was taken to the middle of the quartz cell. The steam was injected into the quartz cell, and the steam flowmeter was used to monitor the steam flux. The remaining testing process in the biphasic system was similar to that of the triphase system hydrogen evolution.

The AQY is calculated based on the formula below⁶⁰:

$$AQY = \frac{2 * n * N_A}{(E * A * T * \lambda) / (h * C)} * 100\% \quad (5)$$

where n is the H₂ yield, N_A is the Avogadro number, E is light intensity, A is the irradiation area, T is the time, λ is the wavelength, h is the Planck constant, and C is the speed of light.

The H₂O₂ concentration was determined through UV-Vis absorption spectra⁶¹. 0.01 mol L⁻¹ copper (II) sulfate solution was prepared in advance, and 1 g neocuproine was dissolved in 100 ml ethanol to obtain 2,9-dimethyl-1,10-phenanthroline (DMP) solution. 5 μmol ml⁻¹ H₂O₂ was used as a standard sample to react with copper (II) sulfate solution and DMP solution. The obtained absorption spectrum was the baseline. Then, the solutions after photocatalytic reaction were mixed with copper (II) sulfate solution and DMP solution to measure related absorption spectra, which could be utilized to calculate the H₂O₂ concentration through comparing with the baseline.

The hydrogen evolution measurement in the wood/photocatalyst photothermal-photocatalytic system was carried out similarly to the triphase reaction measurement. The quartz cell contained 50 ml of deionized water. The wood/photocatalyst systems were floating on the water. The remaining testing process was similar to that of the triphase system hydrogen evolution measurement. In simulated seawater splitting to hydrogen measurement, the simulated seawater contains 3.1 wt% NaCl, 0.2 wt% MgCl₂, and 0.1 wt% KCl; and the wood/photocatalyst systems (0.3 g CuS-MoS₂ were loaded) were floating on the simulated seawater. After the photocatalytic reaction, the hydrogen collector was taken to be measured through gas chromatography. The hydrogen collector was replaced by a new one every 2 h to carry out the photocatalytic stability measurement.

Theoretical calculation. All periodic calculations were performed in the Vienna Ab Initio Simulation Package (VASP), which was on the basis of the generalized gradient approximation (GGA) and the exchange-correlation energy of interacting electrons determined by the revised-Perdew-Burke-Ernzerhof (RPBE) functional. The ion-electron interaction was described with the projector augmented wave (PAW) method⁶². A basis set of plane waves was up to an energy cutoff of 520 eV. The CoO (111) surface was modeled with a 2 × 2 supercell containing 13 atomic layers, where 5 layers were fixed in the bulk positions. All slab structure included a vacuum of 15 Å. The dipole moment correction was considered and added in calculation optimization process. And the antiferromagnetic moment was set up

along the (111) direction. A U value of 4.1 eV was applied to the Co d-states. The Monkhorst-pack method with the centered k-point grid ($4 \times 4 \times 1$) was used for surface calculations, respectively. The convergence threshold for the residual force was set to 0.02 eV \AA^{-1} , and energies have converged within 10^{-5} eV . The model structure schemes and band structures of CoO have been shown in the Supplementary Figs. 33 and 34.

The hydrogen and water adsorption energy on various surfaces is defined as^{63,64}

$$\Delta E_{\text{ads}} = E_{\text{base-H}} - E_{\text{base}} - \frac{1}{2} E_{\text{H}_2} \quad (6)$$

$$\Delta E_{\text{ads}} = E_{\text{base-H}_2\text{O}} - E_{\text{base}} - E_{\text{H}_2\text{O}} \quad (7)$$

where $E_{\text{base-H}}$ and $E_{\text{base-H}_2\text{O}}$ are the total energy of the slab model with H and H_2O adsorption, E_{base} is the energy of a clean slab surface, and E_{H_2} and $E_{\text{H}_2\text{O}}$ are that for hydrogen and water molecules.

The Gibbs energy can be calculated by taking zero-point energy and entropy corrections into account⁶⁵ such that $\Delta G = \Delta E + \Delta E_{\text{ZPE}} - T\Delta S + \Delta G_{\text{pH}}$. Where ΔE_{ZPE} and $T\Delta S$ are the difference in zero-point energy and entropy between the adsorbed species and free species in the gas phase, respectively^{66,67}. At different pH values, $\Delta G_{\text{pH}} = 0.059 \times \text{pH}$. The solvent effect is considered through the implicit solvation model based on the VASPsol^{68,69}. The dielectric constants of liquid water and gas water are indexed to be 81 and 1, respectively. The differences of Gibbs free energies in the bi- and tri-phasic systems are the temperature (373 and 298 K, respectively) and the entropy change ΔS . The dielectric constant and entropy change ΔS correction in the vapor water and liquid water was obtained from the Handbook of Chemistry and Physics⁷⁰. The entropy S is $0.367 \text{ kJ kg}^{-1} \text{ K}^{-1}$ at 298 K under the standard pressure, while at 373 K the entropy S is $1.303 \text{ kJ kg}^{-1} \text{ K}^{-1}$ when the water is liquid (the value is used for Gibbs free energies calculation in tri-phasic systems at 373 K) and $7.361 \text{ kJ kg}^{-1} \text{ K}^{-1}$ when the water is in the gas phase (the value is used for Gibbs free energies calculation in biphasic systems at 373 K).

Data availability

The authors declare that the data supporting the findings of this study are available within this paper and its Supplementary information file, or from the corresponding authors.

Received: 3 June 2020; Accepted: 7 January 2021;

Published online: 26 February 2021

References

- Voiry, D., Shin, H. S., Loh, K. P. & Chhowalla, M. Low-dimensional catalysts for hydrogen evolution and CO_2 reduction. *Nat. Rev. Chem.* **2**, 0105 (2018).
- Chen, S., Takata, T. & Domen, K. Particulate photocatalysts for overall water splitting. *Nat. Rev. Mater.* **2**, 17050 (2017).
- Zhang, J. Q. et al. Single platinum atoms immobilized on an MXene as an efficient catalyst for the hydrogen evolution reaction. *Nat. Catal.* **1**, 985–992 (2018).
- Pinaud, B. A. et al. Technical and economic feasibility of centralized facilities for solar hydrogen production via photocatalysis and photoelectrochemistry. *Energy Environ. Sci.* **6**, 1983–2002 (2013).
- Guo, L. et al. $\text{MoS}_2/\text{TiO}_2$ heterostructures as nonmetal plasmonic photocatalysts for highly efficient hydrogen evolution. *Energy Environ. Sci.* **11**, 106–114 (2018).
- Wang, Q. et al. Scalable water splitting on particulate photocatalyst sheets with a solar-to-hydrogen energy conversion efficiency exceeding 1%. *Nat. Mater.* **15**, 611–615 (2016).
- Liu, M. C. et al. Photocatalytic hydrogen production using twinned nanocrystals and an unanchored NiS_x co-catalyst. *Nat. Energy* **1**, 16151 (2016).
- Dionigi, F. et al. Gas phase photocatalytic water splitting with $\text{Rh}_{2-y}\text{Cr}_y\text{O}_3/\text{GaN}:\text{ZnO}$ in μ -reactors. *Energy Environ. Sci.* **4**, 2937–2942 (2011).
- Kistler, T. A., Um, M. Y. & Agbo, P. Stable photoelectrochemical hydrogen evolution for 1000 h at 14% efficiency in a monolithic vapor-fed device. *J. Electrochem. Soc.* **167**, 066502 (2020).
- Zafeiropoulos, G., Johnson, H., Kinge, S., van de Sanden, M. C. M. & Tsampas, M. N. Solar hydrogen generation from ambient humidity using functionalized porous photoanodes. *ACS Appl. Mater. Inter.* **11**, 41267–41280 (2019).
- Daeneke, T. et al. Surface water dependent properties of sulfur-rich molybdenum sulfides: electrolyteless gas phase water splitting. *ACS Nano* **11**, 6782–6794 (2017).
- Isogai, S. et al. Composite of $\text{Rh}_y\text{Cr}_{2-y}\text{O}_3/(\text{Ga}_{1-x}\text{Zn}_x)(\text{N}_{1-x}\text{O}_x)$ photocatalysts with hydrophobic polytetrafluoroethylene (PTFE) membranes for the fabrication of novel reaction sites for water vapor splitting under visible light. *Catal. Lett.* **143**, 150–153 (2013).
- Yin, Q. Q. et al. Plasmonic molybdenum oxide nanosheets supported silver nanocubes for enhanced near-infrared antibacterial activity: synergism of photothermal effect, silver release and photocatalytic reactions. *Appl. Catal. B-Environ.* **224**, 671–680 (2018).
- Yan, B., Du, C., Lin, Z. Y. & Yang, G. W. Photothermal conversion assisted photocatalytic hydrogen evolution from amorphous carbon nitrogen nanosheets with nitrogen vacancies. *Phys. Chem. Chem. Phys.* **22**, 4453–4463 (2020).
- Lu, L. L., Xu, X. X., An, K. L., Wang, Y. & Shi, F. N. Coordination polymer derived $\text{NiS}@g\text{-C}_3\text{N}_4$ composite photocatalyst for sulfur vacancy and photothermal effect synergistic enhanced H_2 production. *ACS Sustain. Chem. Eng.* **6**, 11869–11876 (2018).
- Jia, C. et al. Rich mesostructures derived from natural woods for solar steam generation. *Joule* **1**, 588–599 (2017).
- Xue, G. et al. Robust and low-cost flame-treated wood for high-performance solar steam generation. *ACS Appl. Mater. Inter.* **9**, 15052–15057 (2017).
- He, S. M. et al. Nature-inspired salt resistant bimodal porous solar evaporator for efficient and stable water desalination. *Energy Environ. Sci.* **12**, 1558–1567 (2019).
- Zhan, X. Y. et al. Efficient CoO nanowire array photocatalysts for H_2 generation. *Appl. Phys. Lett.* **105**, 153903 (2014).
- Shi, W. L. et al. Carbon dots anchored on octahedral CoO as a stable visible-light-responsive composite photocatalyst for overall water splitting. *J. Mater. Chem. A* **37**, 19800–19807 (2017).
- Majumdar, A. Scanning thermal microscopy. *Annu. Rev. Mater. Sci.* **29**, 505–585 (1999).
- Liao, L. et al. Efficient solar water-splitting using a nanocrystalline CoO photocatalyst. *Nat. Nanotechnol.* **9**, 69–73 (2014).
- Gallis, M. A., Torczynski, J. R. & Rader, D. J. Molecular gas dynamics observations of Chapman-Enskog behavior and departures there from in nonequilibrium gases. *Phys. Rev. E Stat. Nonlin. Soft Matter Phys.* **69**, 042201 (2004).
- Fernandez de la Mora, J. & Fernandez-Feria, R. Two-fluid Chapman-Enskog theory for binary gas mixtures. *Phys. Fluids* **30**, 2063 (1987).
- Xie, D. G. et al. In situ study of the initiation of hydrogen bubbles at the aluminium metal/oxide interface. *Nat. Mater.* **14**, 899–903 (2015).
- Pan, Z., Zhang, G. & Wang, X. Polymeric carbon nitride/reduced graphene oxide/ Fe_2O_3 : all-solid-state Z-scheme system for photocatalytic overall water splitting. *Angew. Chem. Int. Ed.* **58**, 7102–7106 (2019).
- Maeda, K., Murakami, N. & Ohno, T. Dependence of activity of rutile titanium(IV) oxide powder for photocatalytic overall water splitting on structural properties. *J. Phys. Chem. C* **118**, 9093–9100 (2014).
- Nakamura, R., Okamura, T., Ohashi, N., Imanishi, A. & Nakato, Y. Molecular mechanisms of photo-induced oxygen evolution, PL emission, and surface roughening at atomically smooth (110) and (100) n-TiO₂ (rutile) surfaces in aqueous acidic solutions. *J. Am. Chem. Soc.* **127**, 12975–12983 (2005).
- Peng, S., Cao, Y., Zhou, F., Xu, Z. & Li, Y. CoP decorated with Co_3O_4 as a cocatalyst for enhanced photocatalytic hydrogen evolution via dye sensitization. *Appl. Surf. Sci.* **487**, 315–321 (2019).
- Zhao, H., Guo, L., Xing, C., Liu, H. & Li, X. A homojunction-heterojunction-homojunction scaffold boosts photocatalytic H_2 evolution over $\text{Cd}_{0.5}\text{Zn}_{0.5}\text{S}/\text{CoO}$ hybrids. *J. Mater. Chem. A* **8**, 1955–1965 (2020).
- Liu, X., Min, S., Wang, F. & Zhang, Z. Confining Mo-activated CoS_x active sites within MCM-41 for highly efficient dye-sensitized photocatalytic H_2 evolution. *J. Colloid Interf. Sci.* **563**, 112–121 (2020).
- Tian, B. et al. Supported black phosphorus nanosheets as hydrogen-evolving photocatalyst achieving 5.4% energy conversion efficiency at 353 K. *Nat. Commun.* **9**, 1397 (2018).
- Peng, R. et al. In-plane heterojunctions enable multiphase two-dimensional (2D) MoS_2 nanosheets as efficient photocatalysts for hydrogen evolution from water reduction. *ACS Catal.* **6**, 6723–6729 (2016).
- Vedhanarayanan, B., Chen, C. C. & Lin, T. W. Plasmon-enhanced photocatalytic hydrogen production by dual dye sensitized ternary composite of MoS_2/Au core-Ag shell nanoparticles/graphene. *J. Power Sources* **477**, 229033 (2020).
- Yu, F. et al. Molecular engineering of donor-acceptor conjugated polymer/ $g\text{-C}_3\text{N}_4$ heterostructures for significantly enhanced hydrogen evolution under visible-light irradiation. *Adv. Funct. Mater.* **28**, 1804512 (2018).
- Jing, H. et al. Precursor-engineering coupled microwave molten-salt strategy enhances photocatalytic hydrogen evolution performance of $g\text{-C}_3\text{N}_4$ nanostructures. *ChemSusChem* **13**, 827–837 (2020).
- Chen, J. et al. Molecular design of polymer heterojunctions for efficient solar-hydrogen conversion. *Adv. Mater.* **29**, 1606198 (2017).
- Li, T. et al. Conductive polymer supported and confined iron phosphide nanocrystals for boosting the photocatalytic hydrogen production of graphitic carbon nitride. *J. Mater. Chem. C* **8**, 14540–14547 (2020).

39. Yuan, W. et al. Laminated hybrid junction of sulfur-doped TiO₂ and a carbon substrate derived from Ti₃C₂ MXenes: toward highly visible light-driven photocatalytic hydrogen evolution. *Adv. Sci.* **5**, 1700870 (2018).
40. Xiao, S. et al. Copper nanowires: a substitute for noble metals to enhance photocatalytic H₂ generation. *Nano Lett.* **15**, 4853–4858 (2015).
41. Xiang, Y. et al. Enhanced visible light photocatalytic activity of TiO₂ assisted by organic semiconductors: a structure optimization strategy of conjugated polymers. *J. Mater. Chem. A* **6**, 153–159 (2018).
42. Xin, X. et al. In-situ growth of high-content 1T phase MoS₂ confined in the CuS nanoframe for efficient photocatalytic hydrogen evolution. *Appl. Catal. B-Environ.* **269**, 118773 (2020).
43. Hong, Y. P. et al. Enhanced visible light photocatalytic hydrogen production activity of CuS/ZnS nanoflower spheres. *J. Mater. Chem. A* **3**, 13913–13919 (2015).
44. Yu, S. et al. Efficient photocatalytic hydrogen evolution with ligand engineered all-inorganic InP and InP/ZnS colloidal quantum dots. *Nat. Commun.* **9**, 4009 (2018).
45. Kosco, J. et al. Enhanced photocatalytic hydrogen evolution from organic semiconductor heterojunction nanoparticles. *Nat. Mater.* **19**, 559–565 (2020).
46. Li, Z. et al. Two-dimensional Janus heterostructures for superior Z-scheme photocatalytic water splitting. *Nano Energy* **59**, 537–544 (2019).
47. Zhang, F. M. et al. Rational design of MOF/COF hybrid materials for photocatalytic H₂ evolution in the presence of sacrificial electron donors. *Angew. Chem. Int. Ed.* **57**, 12106–12110 (2018).
48. Wang, X. et al. Sulfone-containing covalent organic frameworks for photocatalytic hydrogen evolution from water. *Nat. Chem.* **10**, 1180–1189 (2018).
49. Ran, J. et al. 2D metal organic framework nanosheet: a universal platform promoting highly efficient visible-light-induced hydrogen production. *Adv. Energy Mater.* **9**, 1803402 (2019).
50. Xing, M. et al. Spatially separated CdS shells exposed with reduction surfaces for enhancing photocatalytic hydrogen evolution. *Adv. Funct. Mater.* **27**, 1702624 (2017).
51. Lu, Y. et al. Hierarchical CdS/m-TiO₂/G ternary photocatalyst for highly active visible light-induced hydrogen production from water splitting with high stability. *Nano Energy* **47**, 8–17 (2018).
52. Lee, B. H. et al. Reversible and cooperative photoactivation of single-atom Cu/TiO₂ photocatalysts. *Nat. Mater.* **18**, 620–626 (2019).
53. Yu, Y. et al. Surface engineering for extremely enhanced charge separation and photocatalytic hydrogen evolution on g-C₃N₄. *Adv. Mater.* **30**, 1705060 (2018).
54. Meng, N. et al. Engineering oxygen-containing and amino groups into two-dimensional atomically-thin porous polymeric carbon nitrogen for enhanced photocatalytic hydrogen production. *Energy Environ. Sci.* **11**, 566–571 (2018).
55. Zhang, Y. et al. Leaf-mosaic-inspired vine-like graphitic carbon nitride showing high light absorption and efficient photocatalytic hydrogen evolution. *Adv. Energy Mater.* **8**, 1801139 (2018).
56. Zhang, L. et al. Localized surface plasmon resonance enhanced photocatalytic hydrogen evolution via Pt@Au NRs/C₃N₄ nanotubes under visible-light irradiation. *Adv. Funct. Mater.* **29**, 1806774 (2019).
57. Li, Q. Y. & Lu, G. X. Significant effect of pressure on the H₂ releasing from photothermal-catalytic water steam splitting over TiSi₂ and Pt/TiO₂. *Catal. Lett.* **125**, 376–379 (2008).
58. Domen, K., Naito, S., Soma, M., Onishi, T. & Tamaru, K. Photocatalytic decomposition of water-vapor on an NiO-SrTiO₃ catalyst. *J. Chem. Soc. Chem. Comm.* **12**, 543–544 (1980).
59. Ni, G. et al. A salt-rejecting floating solar still for low-cost desalination. *Energy Environ. Sci.* **11**, 1510–1519 (2018).
60. Wang, Y. et al. Linker-controlled polymeric photocatalyst for highly efficient hydrogen evolution from water. *Energy Environ. Sci.* **10**, 1643–1651 (2017).
61. Baga, A. N., Johnson, G. R. A., Nazhat, N. B. & Saadalla-nazhat, R. A. A simple spectrophotometric determination of hydrogen peroxide at low concentrations in aqueous solution. *Anal. Chim. Acta* **204**, 349–353 (1988).
62. Blöchl, P. E. Projector augmented-wave method. *Phys. Rev. B* **50**, 17953–17979 (1994).
63. Rossmeisl, J., Logadottir, A. & Norskov, J. K. Electrolysis of water on (oxidized) metal surfaces. *Chem. Phys.* **319**, 178–184 (2005).
64. Norskov, J. K. et al. Origin of the overpotential for oxygen reduction at a fuel-cell cathode. *J. Phys. Chem. B* **108**, 17886–17892 (2004).
65. Liu, X., Jiao, Y., Zheng, Y., Davey, K. & Qiao, S. Z. A computational study on Pt and Ru dimers supported on graphene for the hydrogen evolution reaction: new insight into the alkaline mechanism. *J. Mater. Chem. A* **7**, 3648–3654 (2019).
66. Jiao, Y., Zheng, Y., Davey, K. & Qiao, S. Z. Activity origin and catalyst design principles for electrocatalytic hydrogen evolution on heteroatom-doped graphene. *Nat. Energy* **1**, 16130–16138 (2016).
67. Zhang, C. et al. Sub-1.1 nm ultrathin porous CoP nanosheets with dominant reactive {200} facets: a high mass activity and efficient electrocatalyst for the hydrogen evolution reaction. *Chem. Sci.* **8**, 2769–2775 (2017).
68. Mathew, K., Sundaraman, R., Letchworth-Weaver, K., Arias, T. A. & Hennig, R. G. Implicit solvation model for density-functional study of nanocrystal surfaces and reaction pathways. *J. Chem. Phys.* **140**, 084106 (2014).
69. Mathew, K., Kolluru, V. S. C., Mula, S., Steinmann, S. N. & Hennig, R. G. Implicit self-consistent electrolyte model in plane-wave density-functional theory. *J. Chem. Phys.* **151**, 234101 (2019).
70. Lide, D. R. *Handbook of Chemistry and Physics* (CRC Press, 2004).

Acknowledgements

This research is supported by the Basic Research Fund for Free Exploration in Shenzhen (Grant No. JCYJ20180306171402878), the project of Shaanxi Young Stars in Science and Technology (2017KJXX-18), the Shaanxi International Cooperation Project (2020KWZ-018), and the Fundamental Research Funds for the Central Universities (3102019ghxm003, 3102019JC005, 3102019ghjd001). We thank the members from the Analytical & Testing Center of Northwestern Polytechnical University for the help of TEM and XPS characterization. We also thank Prof. Weihong Qi, Prof. Qingfeng Zeng, and Prof. Junjie Wang for valuable discussion about the theoretical calculation.

Author contributions

B.W. and X.L. conceived the concept and directed the research. S.G. and X.L. designed the project. S.G. carried out material synthesis and related characterization tests. J.L. gave advice on the experiments. S.G., X.L., and B.W. wrote the paper. All authors discussed the results and commented on the paper.

Competing interests

The authors declare no competing interests.

Additional information

Supplementary information The online version contains supplementary material available at <https://doi.org/10.1038/s41467-021-21526-4>.

Correspondence and requests for materials should be addressed to X.L. or B.W.

Peer review information *Nature Communications* thanks Harald Oberhofer for their contributions to the peer review of this work. Peer review reports are available.

Reprints and permission information is available at <http://www.nature.com/reprints>

Publisher's note Springer Nature remains neutral with regard to jurisdictional claims in published maps and institutional affiliations.



Open Access This article is licensed under a Creative Commons Attribution 4.0 International License, which permits use, sharing, adaptation, distribution and reproduction in any medium or format, as long as you give appropriate credit to the original author(s) and the source, provide a link to the Creative Commons license, and indicate if changes were made. The images or other third party material in this article are included in the article's Creative Commons license, unless indicated otherwise in a credit line to the material. If material is not included in the article's Creative Commons license and your intended use is not permitted by statutory regulation or exceeds the permitted use, you will need to obtain permission directly from the copyright holder. To view a copy of this license, visit <http://creativecommons.org/licenses/by/4.0/>.

© The Author(s) 2021

Supplementary Information for

**Boosting Photocatalytic Hydrogen Production from Water by Photothermally
Induced Biphasic Systems**

Shaohui Guo¹, Xuanhua Li^{1*}, Ju Li², and Bingqing Wei^{3*}

¹State Key Laboratory of Solidification Processing, Center for Nano Energy Materials, School of Materials Science and Engineering, Northwestern Polytechnical University, Xi'an, 710072, China.

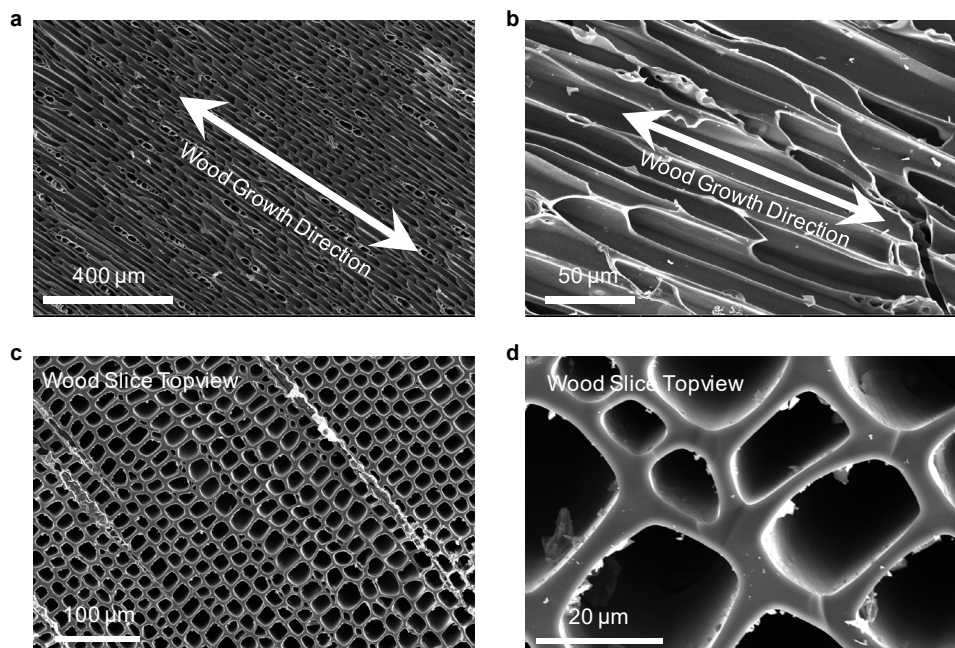
²Department of Nuclear Science and Engineering, Massachusetts Institute of Technology, Cambridge, MA, 02139, USA

³Department of Mechanical Engineering, University of Delaware, Newark, DE19716, USA

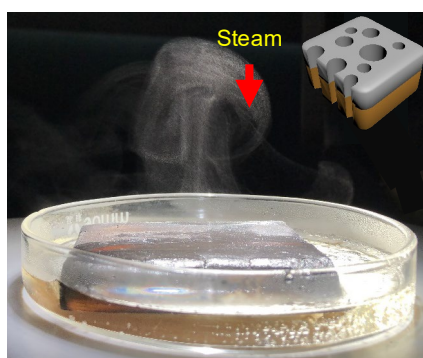
* Corresponding author E-mail:

Xuanhua Li lixh32@nwpu.edu.cn

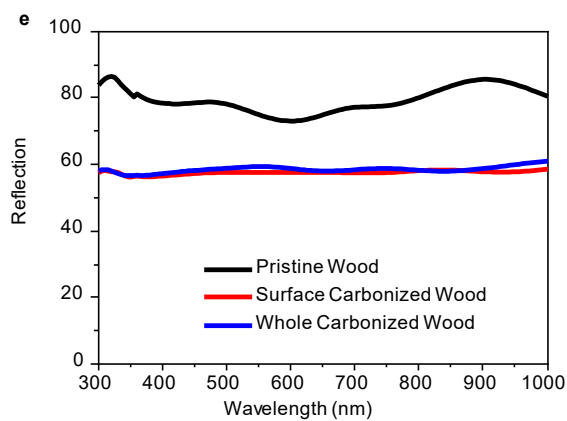
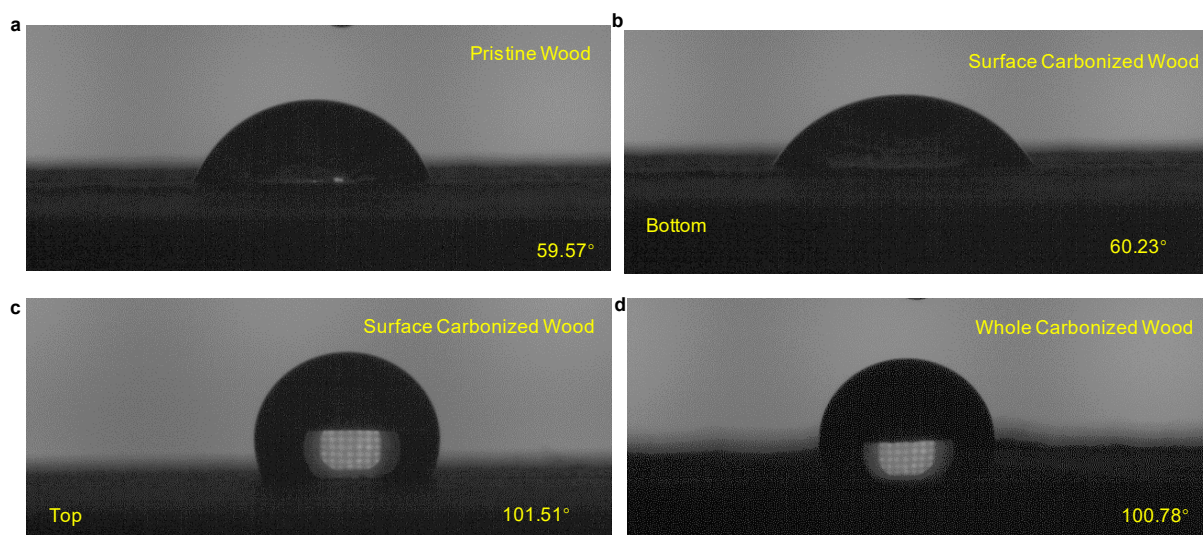
Bingqing Wei weib@udel.edu



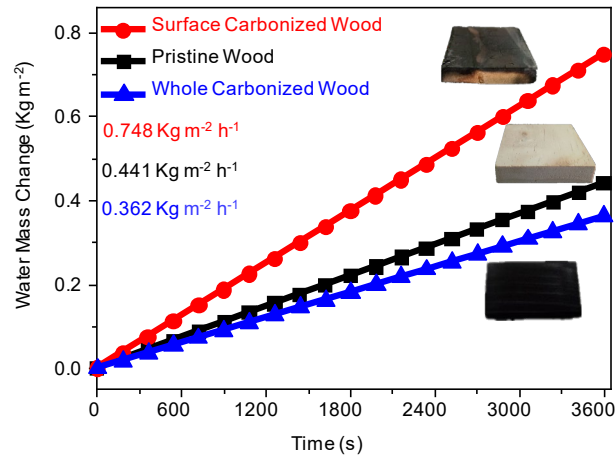
Supplementary Figure 1. SEM images of the wood slice. **a, b** Sideview SEM images of a pinewood. The pinewood growth direction has been observed. **c, d** Topview SEM images of the wood slice, which is cut from a tree perpendicular to its growth direction.



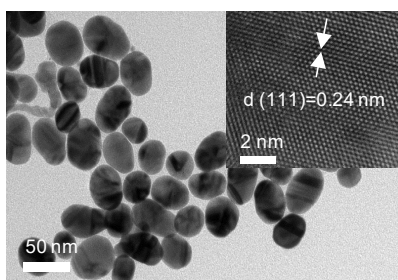
Supplementary Figure 2. Photograph of steam generation process from the surface carbonized wood under light illumination.



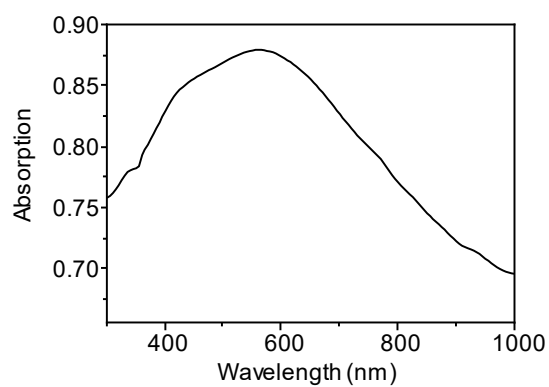
Supplementary Figure 3. a-d The contact angle measurement from the pristine wood, surface carbonized wood, and whole carbonized wood. e The reflection spectra of the pristine wood, surface carbonized wood, and whole carbonized wood.



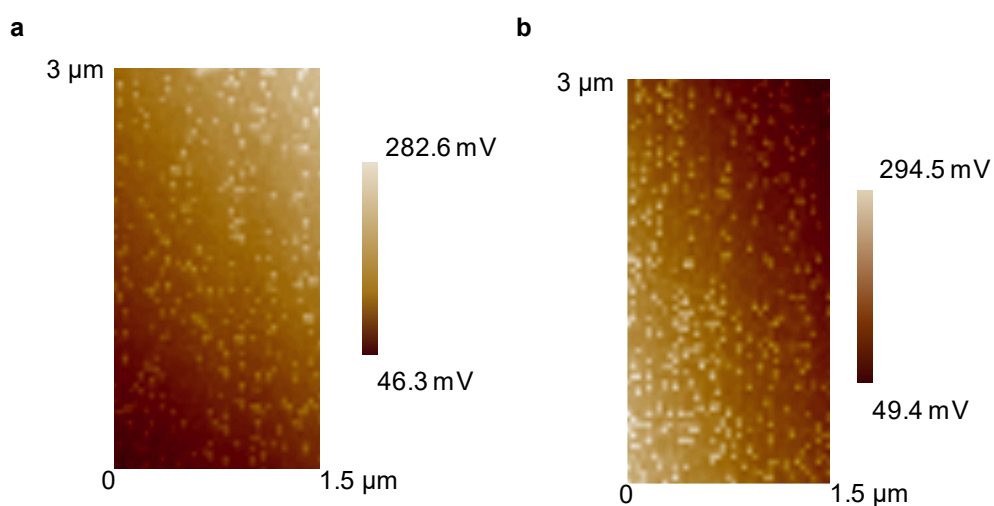
Supplementary Figure 4. Steam evaporation from wood induced mass changes in the water as a function of time. The inset image is the photograph of the pristine wood, surface carbonized wood, and whole carbonized wood. The surface carbonized wood shows the highest steam generation ability among three samples because of the good light absorptivity and the hydrophilic wood structure at the bottom.¹ The solar-to-steam conversion efficiencies of the pristine wood, surface carbonized wood, and whole carbonized wood are 27.65 %, 46.90 %, and 22.71 %, respectively.



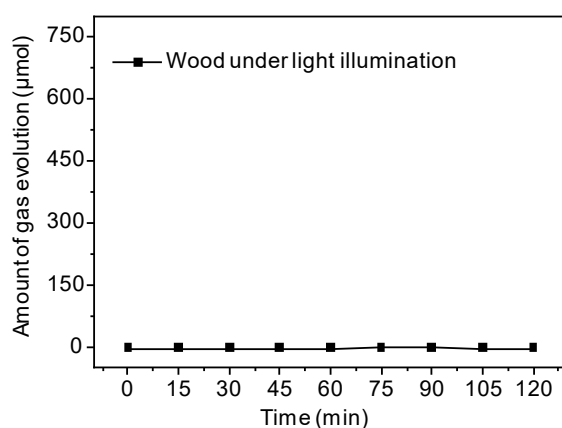
Supplementary Figure 5. TEM image of CoO NPs. Inset: HRTEM image of a CoO NP.



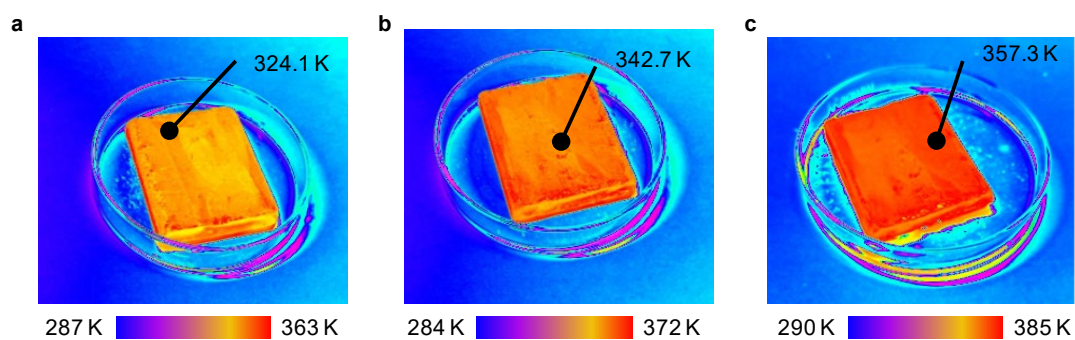
Supplementary Figure 6. The absorption spectra of CoO NPs.



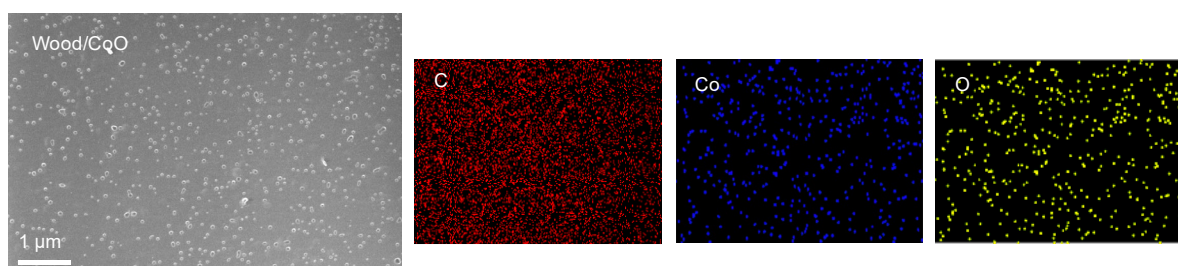
Supplementary Figure 7. **a** The potential of wood/CoO at 300 K, **b** the potential of wood/CoO at 308 K.



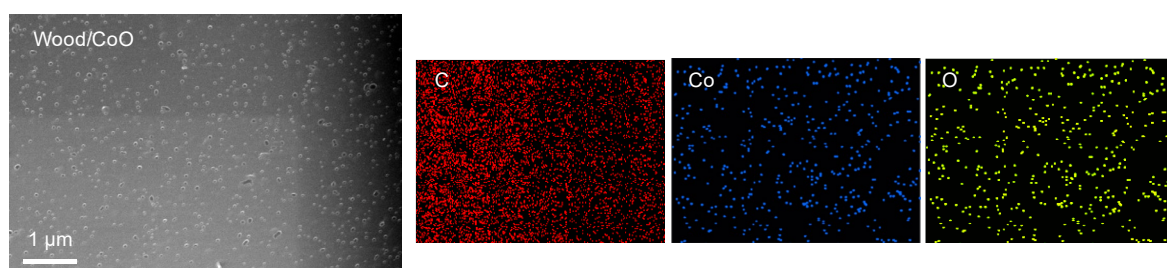
Supplementary Figure 8. Time-dependent photocatalytic gas production profile of the wood under light illumination.



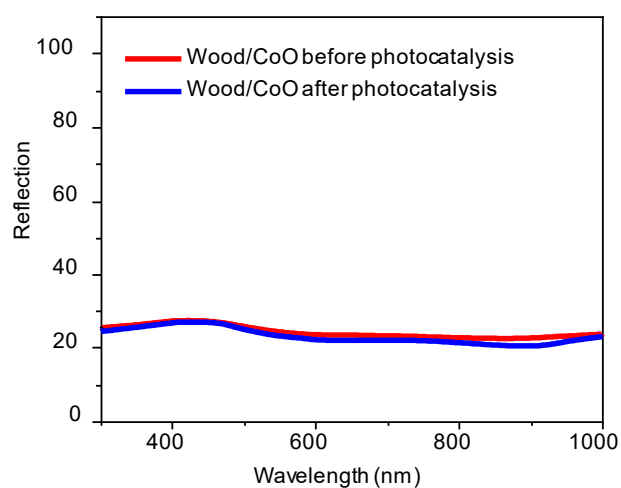
Supplementary Figure 9. Infrared radiation thermal images of the wood/CoO system under light illumination with different solar intensity. **a** 100 mW cm⁻², **b** 200 mW cm⁻², **c** 300 mW cm⁻².



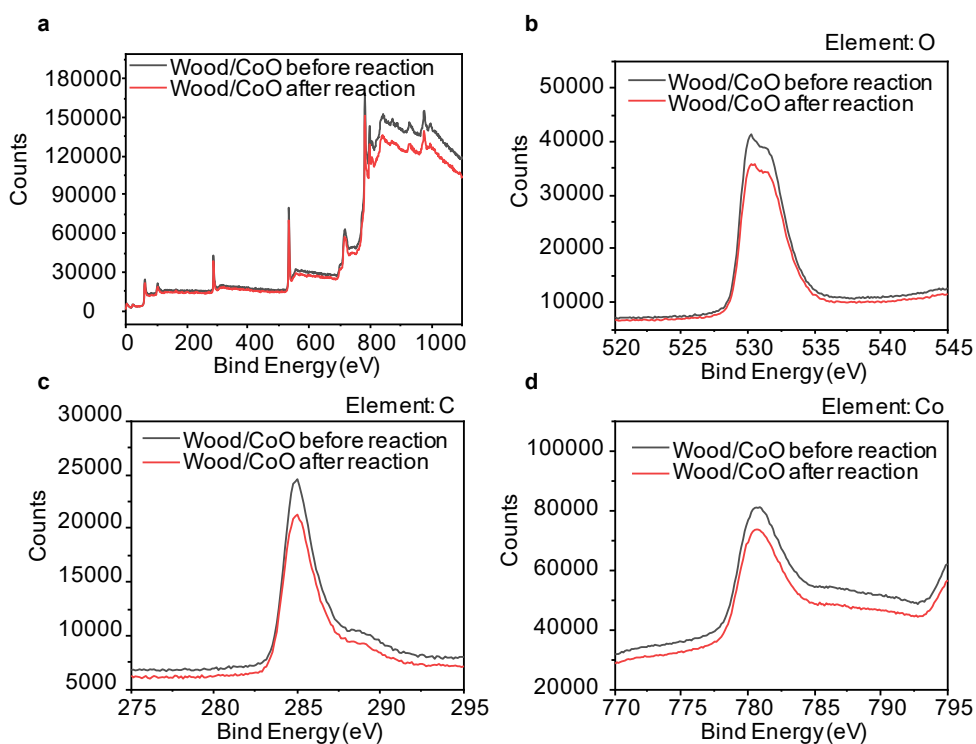
Supplementary Figure 10. SEM images and EDS element mapping of CoO NPs attached to the walls of the wood microchannels before photocatalytic reaction.



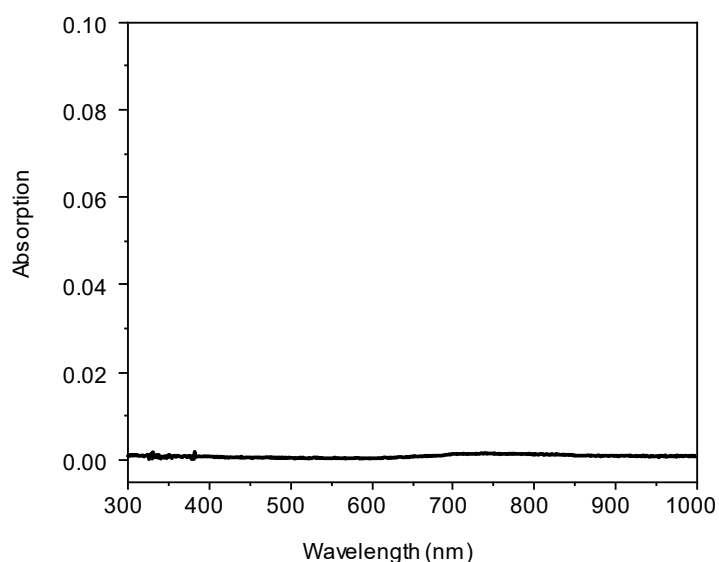
Supplementary Figure 11. SEM images and EDS element mapping of CoO attached to the walls of the wood microchannels after the photocatalytic reaction.



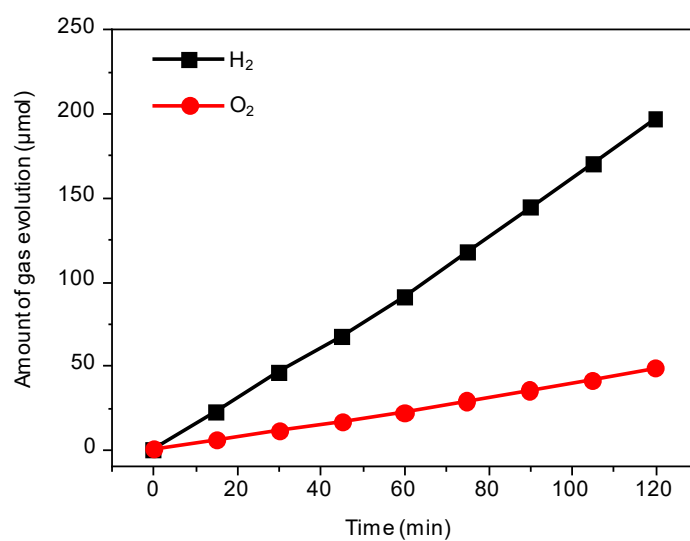
Supplementary Figure 12. The reflection spectra wood/CoO system before and after photocatalysis process.



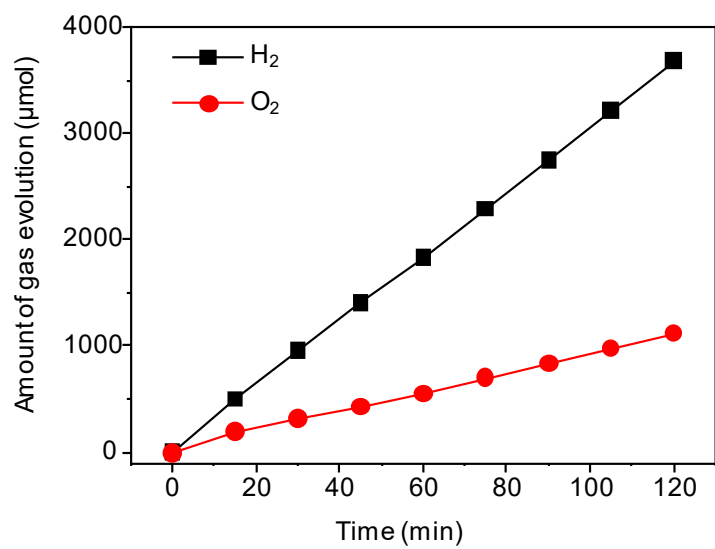
Supplementary Figure 13. The XPS spectra wood/CoO system before and after the photocatalysis process. **a** XPS full spectrum of the wood/CoO system before/after the reaction, **b** high-resolution XPS of element O, **c** high-resolution XPS of element C, and **d** high-resolution XPS of element Co for the wood/CoO system.



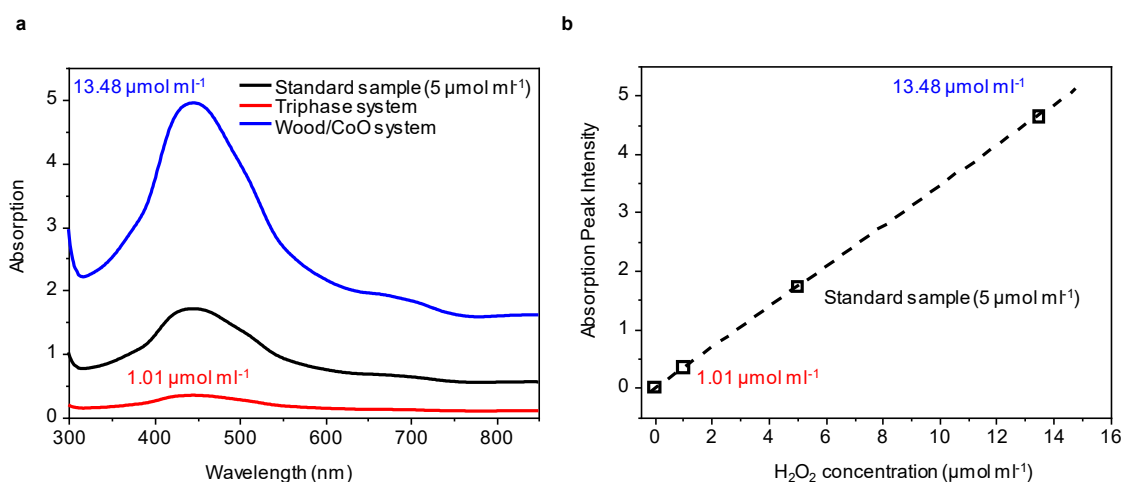
Supplementary Figure 14. The absorption spectrum from bulk water in the wood/CoO system after photocatalytic reaction.



Supplementary Figure 15. Time-dependent photocatalytic gas production profiles from the liquid water. The photocatalyst is CoO NPs, and the sacrificial agent is not added.



Supplementary Figure 16. Time-dependent photocatalytic gas production profiles from the wood/CoO.



Supplementary Figure 17. The H₂O₂ concentration determination from absorption spectra. **a** the absorption spectra from different H₂O₂ concentration, and **b** the linear fitting between absorption peak and H₂O₂ concentration.

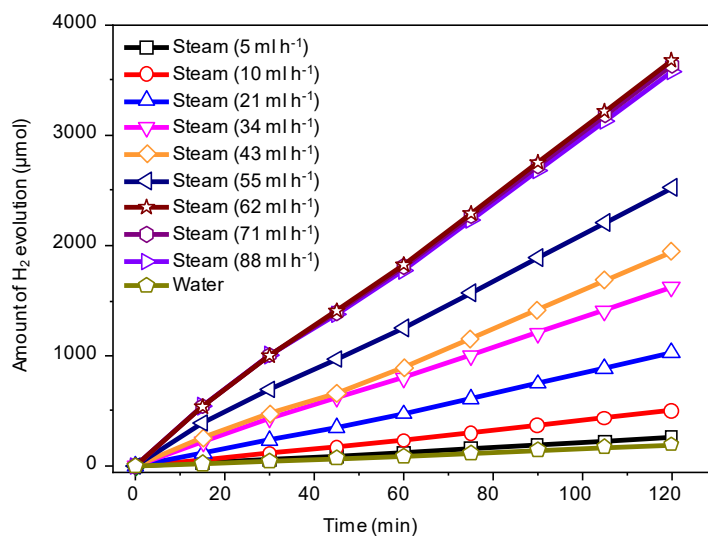
The 5 μmol ml⁻¹ H₂O₂ was used as the standard sample to react with copper (II) sulfate solution and 2,9-dimethyl-1,10-phenanthroline (DMP) solution, and the obtained absorption spectrum was used as the baseline. Due to the linear relationship between absorption peak and H₂O₂ concentration², the H₂O₂ concentration in the solution after the photocatalytic reaction could be calculated based on the above absorption spectra. After the photocatalytic reaction, the concentration of H₂O₂ measured is about 1.01 and 13.48 μmol ml⁻¹ for the triphase reaction system and wood/CoO systems, respectively.

In the triphase reaction system, after 120 min test, the amount of H₂ evolution is about 196.98 μmol, and the amount of O₂ evolution is about 48.04 μmol. After the reaction, the H₂O₂ concentration is 1.01 μmol ml⁻¹ in 100 ml reaction solvent. Thus the amount of H₂O₂ is 101 μmol. The H₂O₂ converts to the O₂ following the reaction equation below:

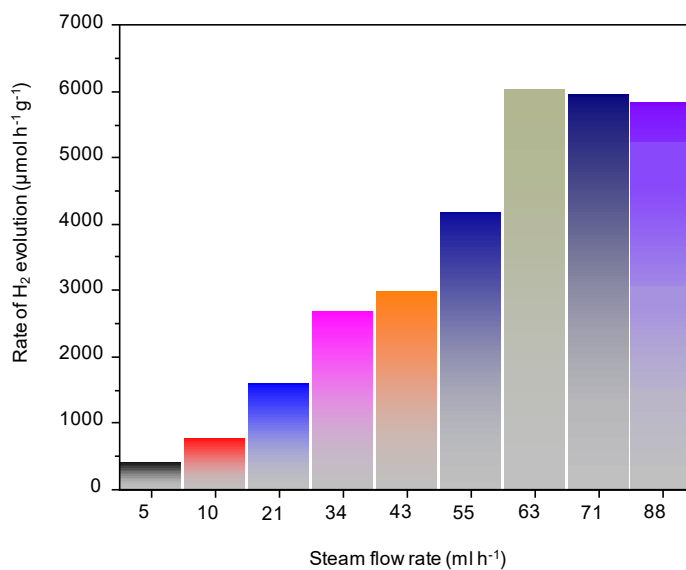


Combing the amount of directly produced O₂ (48.04 μmol) and the amount of indirectly converted O₂ from H₂O₂ (50.50 μmol), the total amount of O₂ is 98.54 μmol. Thus, the production ratio of H₂ and O₂ is 196.68:98.54 (i.e., 1.99:1).

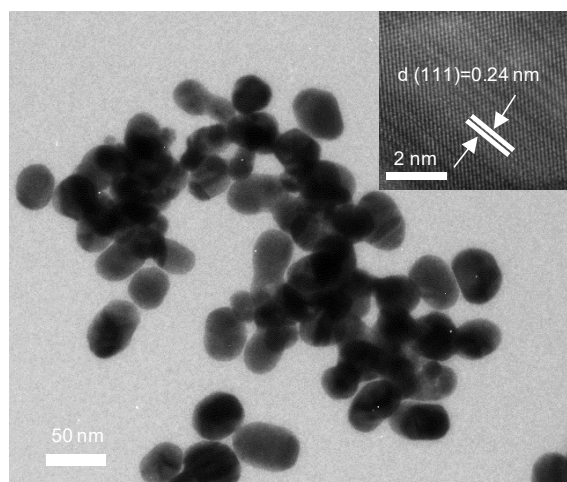
Regarding the wood/CoO system, the amount of H₂ evolution is about 3677.55 μmol, and the amount of O₂ evolution is about 1121.21 μmol after 120 min test. The H₂O₂ concentration is 13.48 μmol ml⁻¹ in 100 ml reaction solvent after the catalytic reaction. Thus, the amount of H₂O₂ is 1348 μmol. Combing the amount of directly produced O₂ (1121.21 μmol) and the amount of indirectly converted O₂ from H₂O₂ (674 μmol), the total amount of O₂ is 1795.21 μmol. Thus, the converted amount of O₂ is 1795.21 μmol. Considering the above calculation, the production ratio of H₂ and O₂ is 3677.55:1795.21 (i.e., 2.04:1).



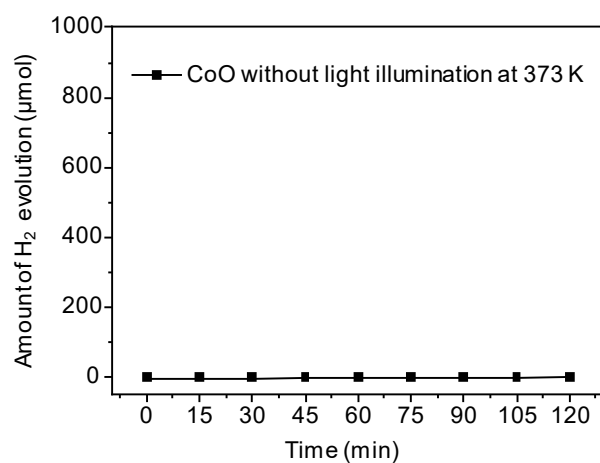
Supplementary Figure 18. Time-dependent photocatalytic hydrogen gas production profiles from the liquid water and water steam with different flow rates. The photocatalyst is CoO NPs.



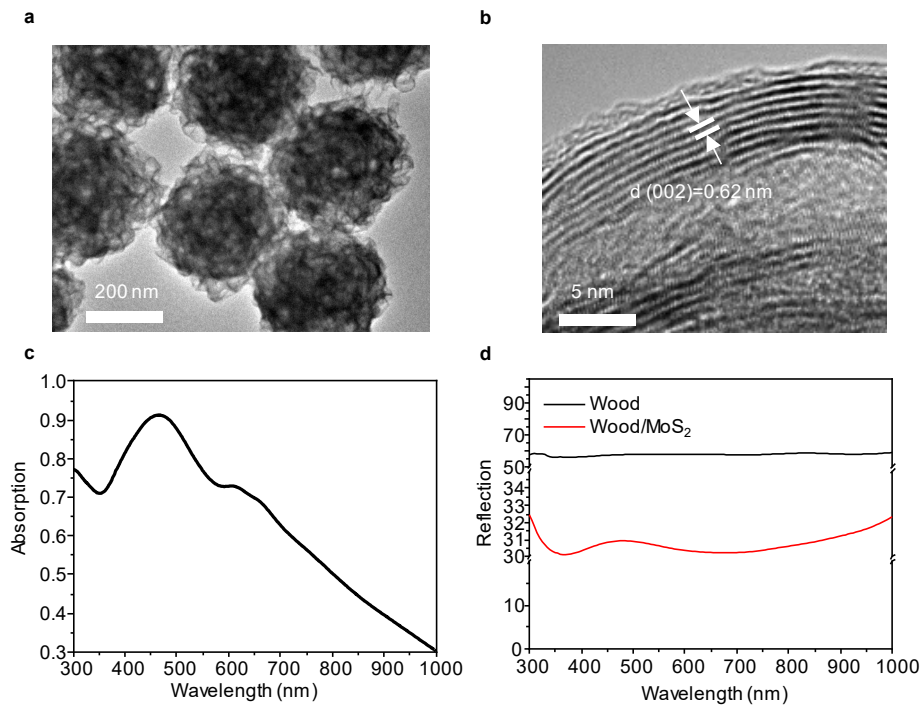
Supplementary Figure 19. The hydrogen production rate as a function of flow rate of the water steam. The photocatalyst is CoO NPs.



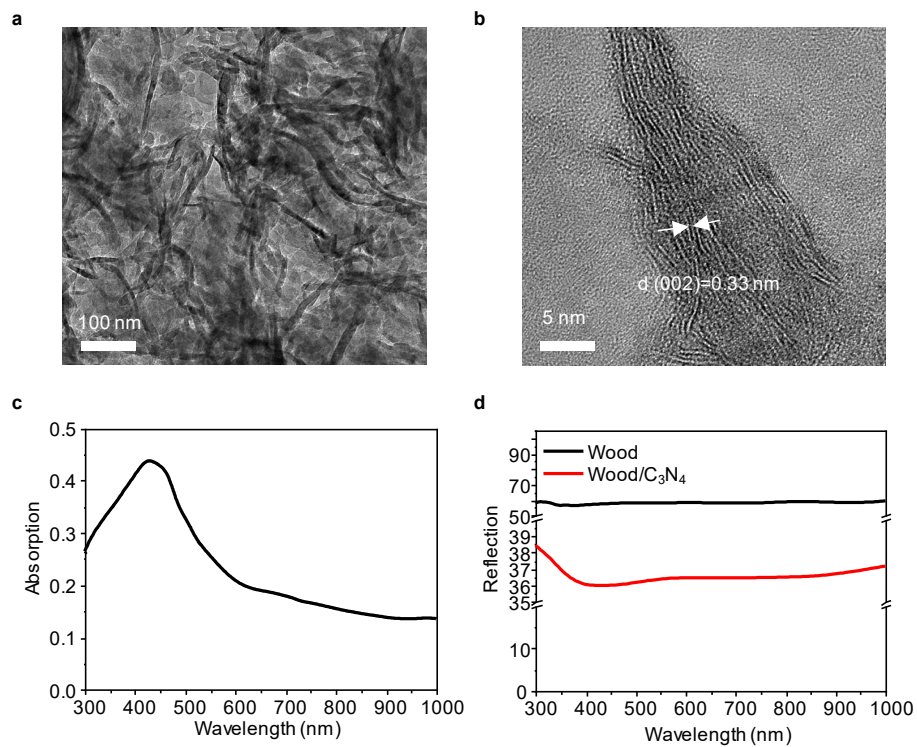
Supplementary Figure 20. TEM image of CoO NPs after the photocatalytic reaction. Inset: HRTEM image of a CoO NP.



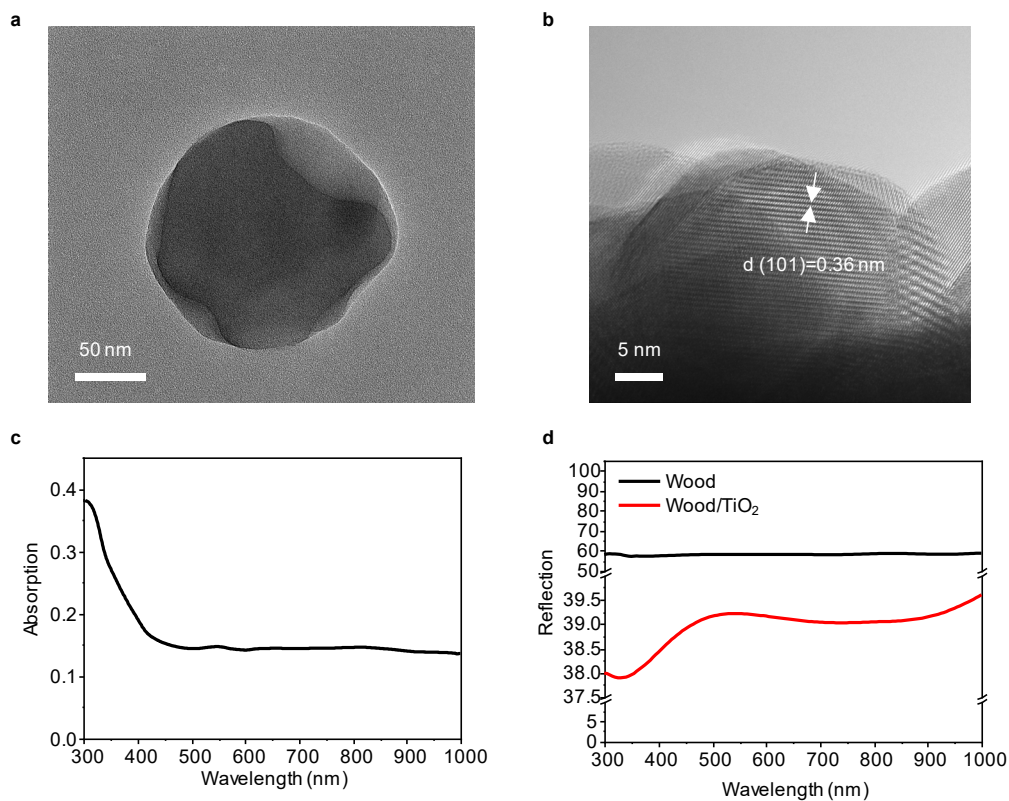
Supplementary Figure 21. Time-dependent photocatalytic hydrogen gas production profile from liquid water at the reaction temperature of 373 K without light illumination.



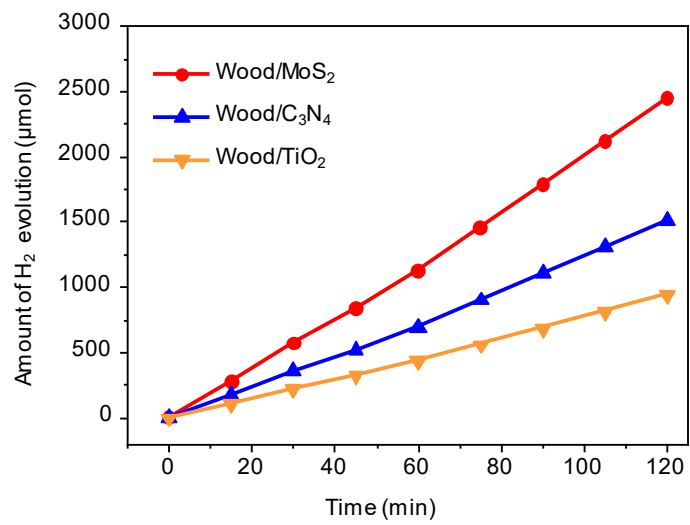
Supplementary Figure 22. **a** TEM image of MoS₂. **b** HRTEM image of MoS₂. **c** The absorption spectrum of MoS₂. **d** Reflection spectra of the wood and wood/MoS₂ system.



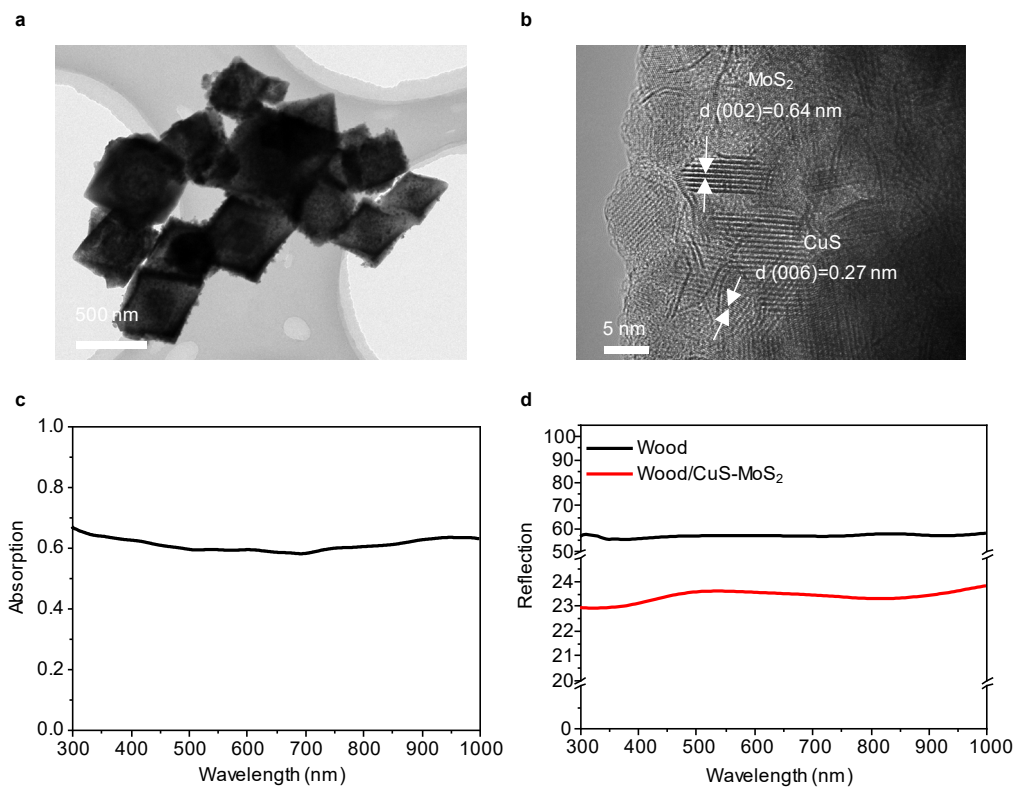
Supplementary Figure 23. **a** TEM image of C_3N_4 . **b** HRTEM image of C_3N_4 . **c** The absorption spectrum of C_3N_4 . **d** Reflection spectra of the wood and wood/ C_3N_4 system.



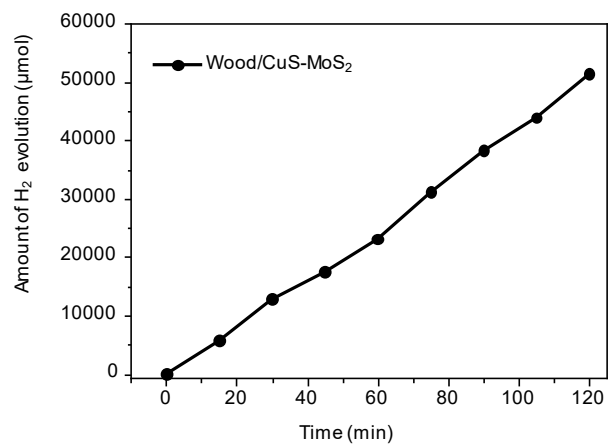
Supplementary Figure 24. **a** TEM image of TiO₂. **b** HRTEM image of TiO₂. **c** The absorption spectrum of TiO₂. **d** Reflection spectra of the wood and wood/TiO₂ system.



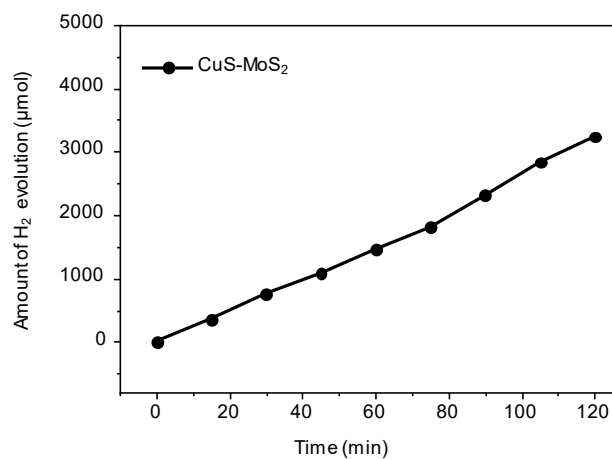
Supplementary Figure 25. Amount of hydrogen production for the wood/MoS₂, wood/C₃N₄, and wood/TiO₂ system.



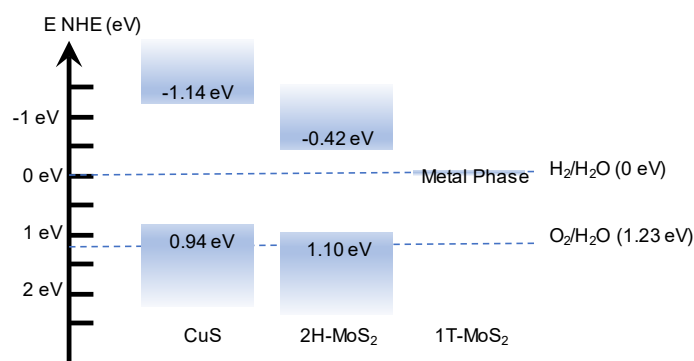
Supplementary Figure 26. **a** TEM image of CuS-MoS₂. **b** HRTEM image of CuS-MoS₂. **c** The light absorption spectra of CuS-MoS₂. **d** Reflection spectra of the wood and wood/CuS-MoS₂ system.



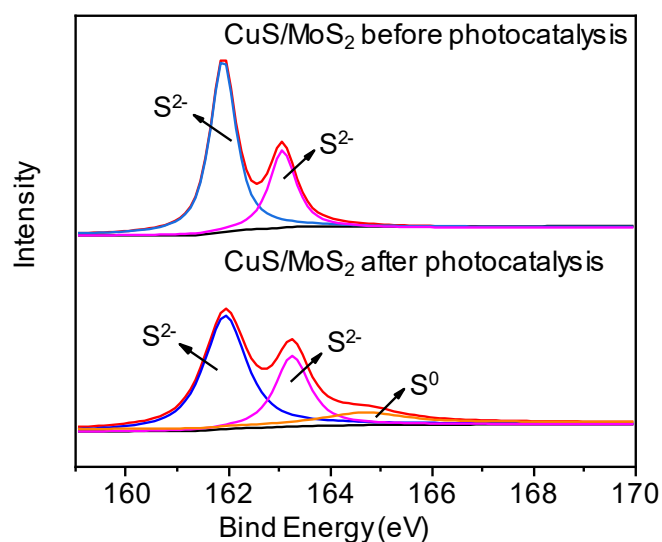
Supplementary Figure 27. Amount of hydrogen production for the biphasic wood/CuS-MoS₂ system without a sacrificial agent.



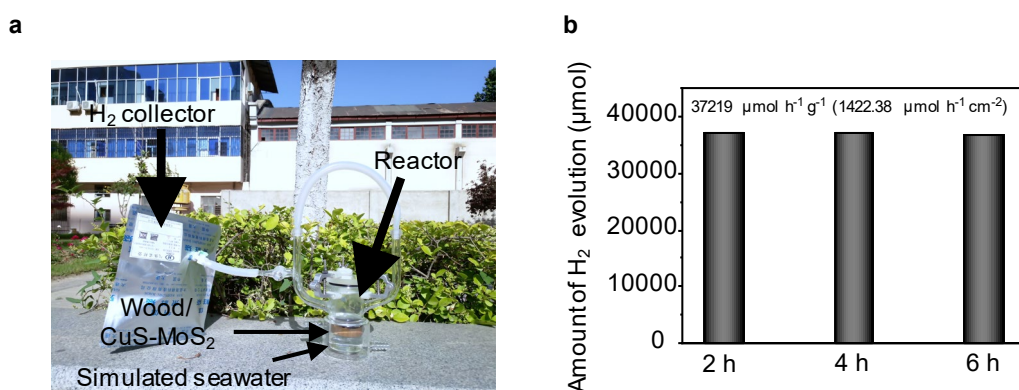
Supplementary Figure 28. Amount of hydrogen production for the triphasic CuS-MoS₂ system without a sacrificial agent.



Supplementary Figure 29. Scheme of energy band positions of CuS-MoS₂ photocatalyst.³



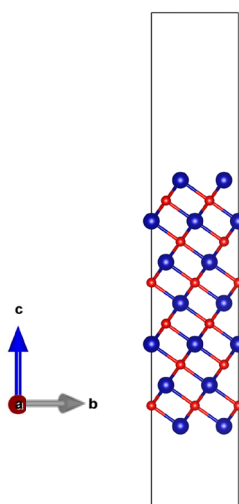
Supplementary Figure 30. The high-resolution XPS of element S for CuS/MoS₂ before and after photocatalytic reaction.



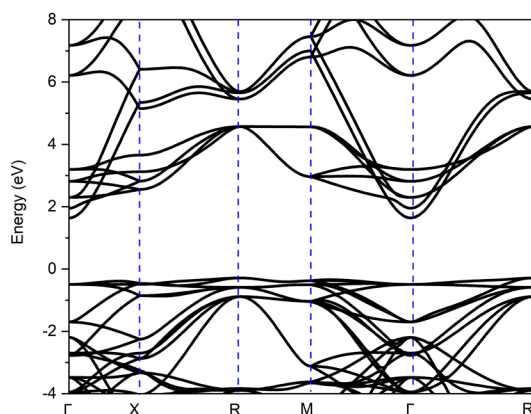
Supplementary Figure 31. Hydrogen evolution for the biphasic wood/CuS-MoS₂ system in simulated seawater. **a** Photograph of hydrogen evolution for the biphasic wood/CuS-MoS₂ architecture in simulated seawater under the illumination of sunshine. **b** Rate of H₂ evolution from the biphasic wood/CuS-MoS₂ system in simulated seawater. The H₂ collector was replaced by a new one every two hours to extract the gas, which was then introduced to the GC device for evaluating the H₂ production.



Supplementary Figure 32. The photograph of the light intensity measurement.



Supplementary Figure 33. The model structure schemes of CoO



Supplementary Figure 34. The band structures of CoO

Supplementary Table 1. The element Co concentration in the bulk water from the wood/CoO system after the photocatalytic reaction based on ICP measurement. Three samples are tested.

	Sample Test 1	Sample Test 2	Sample Test 3
Element Co Concentration ($\mu\text{g ml}^{-1}$)	0.0102	0.0123	0.0088

Supplementary Table 2. The measurement information for AQY calculation, including catalysts, wavelength, light intensity, and H₂ yield.

Catalysts	Wavelength (nm)/ Light intensity (mW cm^{-2})	H ₂ yield (μmol)/ AQY (%)
Wood/CoO	380/13.82	255.01/41.1
Wood/CoO	420/16.32	405.85/50.1
Wood/CoO	500/12.32	325.77/44.8
Wood/MoS ₂	380/13.77	195.87/31.7
Wood/MoS ₂	420/16.59	295.25/35.9
Wood/MoS ₂	500/11.97	223.16/31.5
Wood/C ₃ N ₄	380/13.63	122.67/20.0
Wood/C ₃ N ₄	420/16.12	273.49/34.2
Wood/C ₃ N ₄	500/12.43	175.35/23.9
Wood/TiO ₂	360/13.54	193.74/33.6
Wood/TiO ₂	380/16.87	90.24/11.9

References

- 1 Xue, G. et al. Robust and low-cost flame-treated wood for high-performance solar steam generation. *ACS Appl. Mater. Inter.* **9**, 15052-15057 (2017).
- 2 Baga, A. N., Johnson, G. R. A., Nazhat, N. B. & Saadalla-nazhat, R. A. A simple spectrophotometric determination of hydrogen peroxide at low concentrations in aqueous solution. *Anal. Chim. Acta* **204**, 349-353 (1988).
- 3 Xin, X. et al. In-situ growth of high-content 1T phase MoS₂ confined in the CuS nanoframe for efficient photocatalytic hydrogen evolution. *Appl. Catal. B-Environ.* **269**, 118773 (2020).

Reviewers' comments:

Reviewer #1 (Remarks to the Author):

In this work, the author proposed a new strategy to advance the photocatalytic performance of photocatalysts for the hydrogen production from water, in which solar energy is used to evaporate the water to produce vapor and H₂ can be produced by the photocatalytic reaction of vapor. The highly efficient hydrogen production should be attributed to the reduced interface barrier in the adsorption and transport resistance in this biphasic system with respect to the case that catalytic reaction is performed in bulk water. This work shows some potential in the advance of hydrogen production from water using solar energy. Here are some comments:

- 1) Since the adsorption of vapor is of significance to the production of hydrogen and this process is likely to be governed by the flow rate of the steam. Therefore, it is essential to add some discussions on the relation between the steam flow rate and hydrogen production rate.
- 2) In the catalysis process, H₂O₂ was produced from water, and these H₂O₂ is able to be accumulated on the surface of the wood. Will these accumulated H₂O₂ have any effect on the durability of the device when it was maintained under illumination for a long period (e.g. 8 h for 5 days)?
- 3) The catalyst was spin coated on the surface of the wood, so will the catalyst be very easy to detach from the substrate? This might cause the loss of the catalyst, resulting in the contamination of bulk water.
- 4) The catalytic reactivity of the photocatalytic reaction is related to the solar intensity and reaction temperature. Therefore, the solar intensity might not be in a linear relation with the hydrogen production rate. Their relationship need to be further explored.

Reviewer #2 (Remarks to the Author):

The manuscript describes an experimental study on the photothermal-photocatalytic properties of wood/CoO composite materials. The authors extensively discuss the hydrogen evolution rates of the prepared material, the influence of the state of water (liquid vs. gas) and try to reveal the universality of the approach by utilization of various light-absorbing materials. As such applying photothermal transpiration to produce (solar) steam without additional energy input is quite interesting but the reported data raise some questions. Particularly, the absence of stoichiometric amounts of oxygen (or hydrogen peroxide) are indicative for either a sacrificial reagent (e.g. the wood) participating in the reaction or the general instability of the CoO and particularly the CuS/MoS₂ catalyst where it is even highlighted that NO₂/H₂O₂ has been detected; so what is oxidized in this case? Therefore, claiming overall water splitting is not justified and any comparison with other systems performing overall water splitting is meaningless. Additionally, it is widely accepted in photocatalysis that a comparison photocatalysts based on production rates should be avoided. Instead QY or AQY should be reported. It is also advised to report rates here on a per cm² basis rather than a per g basis given the significant dimensions of the wood used. Generally, it is advised to thoroughly reconsider the wording, i.e. record-high hydrogen production. Additional minor details are:

- The authors suggest stability of the system based on (HR)TEM data. However, comparing Fig S5 and S14 significant agglomeration is evident and the surface of the particles seems to be less ordered. Given that the wood substrate is essential a thorough characterization is required. This should be included and stability of the system clarified.
- It is not clear whether only steam is reacting to H₂ or also liquid water is involved in the reaction. Given that hydrogen peroxide is detected in the liquid phase it might be the later. The author should provide a concise picture illustration the processes occurring.
- The dependence of CoO loading should be addressed. Is this this an optimized configuration?
- The authors report that a solar simulator is used placed 7 cm above the sample. However, it is not

clear whether 100 mW/cm² are obtained at the sample surface.

- The authors report thermal images and indicate that only a minor increase in temperature is observed at the surface of the wood/CoO system. The local temperature at the nm scale (size of the CoO particles) however might be much higher. The authors should comment on local vs. global temperature effects.

- The authors should use appropriate and original literature, i.e. techno-economics used to justify the benefits of a PC system are not reported in Ref. 2. Additionally it is questionable whether the techno-economics of a PC system are actually applicable in this case as the reactor design and dimensions are significantly deviating from a true PC system.

Given the above I would recommend NOT to publish the manuscript in Nature Communications. Major revisions and a significant modification, including discussion of additional data concerning stability, is required before resubmission and additional review.

Reviewer #3 (Remarks to the Author):

In the present manuscript the authors add a novel twist to the by now well known class of carbon-supported nanoparticle catalysts where, instead of using a well defined carbon material, they use charred wood. While this unquestionably makes the whole setup much less well defined than even mesoporous carbon supports, they were able to show that this setup leads to tremendously improved hydrogen production rates in photo-catalytic water splitting. The effect of the charred wood thereby seems to be the fact that it produces water vapour near the catalytic nanoparticles which then favourably influences the overall reaction rates. Given that humanity is still on the hunt for adequate alternative energy production methods and storage media, the discovery of a novel photocatalyst for water splitting is in principle of utmost importance. All the more so considering the ubiquity of the new support material.

Due to my background in theory I do not think my opinion on the experimental methods used in this work will be necessary. I will, however, comment on the theoretical calculations the authors conducted, which, frankly, are so far below the current state of the art to render the results essentially meaningless. As I will outline in detail below, I do not think that any of the calculations undertaken here are of sufficient predictive quality, which to be honest also would make me somewhat suspicious of the rest of the work.

These are the specific problems I found with the manuscript:

- 1) The structural model. Which slab did the authors use, was it a surface unitcell or a supercell, how many layers did they include? This is really the most basic information and the authors fail to give it.
- 2) I assume, because it is never actually stated, that the authors simulated CoO in its rocksalt structure. In which case the O-terminated (111) facet is actually partially charged, meaning their simulation cell should (if they simulated stoichiometric CoO, also not stated) show a quite sizeable dipole perpendicular to the surface. This is well known and most works compensate for this, yet there is no mention of such a compensation in this work.
- 3) One possibility why the authors did not encounter a surface dipole is because the PBE functional used in this work likely yields a metallic electronic structure for CoO. Not knowing the specifics, I would nevertheless assume that their material has a band gap, otherwise it would not be a photocatalyst. Again, this is a well known and understood failure of GGA functionals. Yet, with such a broken electronic structure I do not think that the calculated binding energies show anything but a fortuitous overlap with reality.
- 4) Why did the authors simulate the de-protonated CoO facet? What pH are they aiming for? Most studies nowadays at least try to determine the protonation state of their surface (which btw. could be one way to avoid the aforementioned surface dipole) beforehand.

5) It is completely unclear to me how the authors are supposed to have calculated the Gibbs free energies in the bi- and tri-phasic systems. Did they actually include solvent effects? If so, how? As it is, the way Figure 3c came to be is entirely unclear to me.

6) In order to determine some of the Gibbs free energies, the authors apply a technique now known as the computational hydrogen electrode, by J. Norskov and J. Rossmeisl (eq. 5 in the present work). While this is indeed state of the art, I find it mildly suspicious that the authors neglect to cite any of the original works here.

7) Finally, not a point directly related to the first-principles calculations, but with eq. 1 the authors calculate the effective free energy barrier of their reaction, yet fail to use it for anything than mildly extrapolating towards higher temperatures. Why is this barrier not discussed or at least compared to other setups? I am sure the kinetic barriers on pristine CoO can by now be found in the literature.

These 7 points together paint a very grim picture of at least the theoretical parts of this manuscript. I thus cannot recommend its publication in Nature Communications, or indeed anywhere else.

Point-by-point Response to the Reviewers' Comments

Reviewer #1

In this work, the author proposed a new strategy to advance the photocatalytic performance of photocatalysts for the hydrogen production from water, in which solar energy is used to evaporate the water to produce vapor and H₂ can be produced by the photocatalytic reaction of vapor. The highly efficient hydrogen production should be attributed to the reduced interface barrier in the adsorption and transport resistance in this biphasic system with respect to the case that catalytic reaction is performed in bulk water. This work shows some potential in the advance of hydrogen production from water using solar energy. Here are some comments:

1) Since the adsorption of vapor is of significance to the production of hydrogen and this process is likely to be governed by the flow rate of the steam. Therefore, it is essential to add some discussions on the relation between the steam flow rate and hydrogen production rate.

Response: Thanks very much for the valuable suggestion. The hydrogen production rate as a function of flow rate the water steam (from 5 ml/h to 88 ml/h), as shown in Figure R1, can be easily calculated from the photocatalytic hydrogen gas yield in Figure R2, which was provided as Figure S13 in the original submission. The rate of hydrogen production from steam increases along with the increase of steam flow rate from 5 ml/h to 62 ml/h and is then stabilized when the steam flow rate is further increased. This is because more water molecules are needed to participate in the

hydrogen evolution reaction until saturation is reached, i.e., the optimal steam flow rate is about 62 ml/h.

In the revised version, this discussion has been added in the main text; and Figure R 1 is added as Supplementary Figure 18 in the Supporting Information.

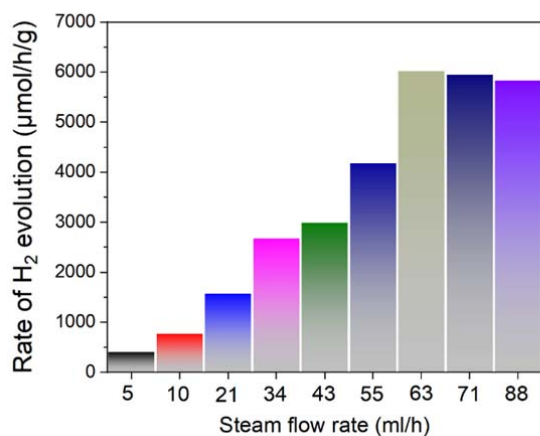


Figure R1. The hydrogen production rate from the water steam with different flow rates.

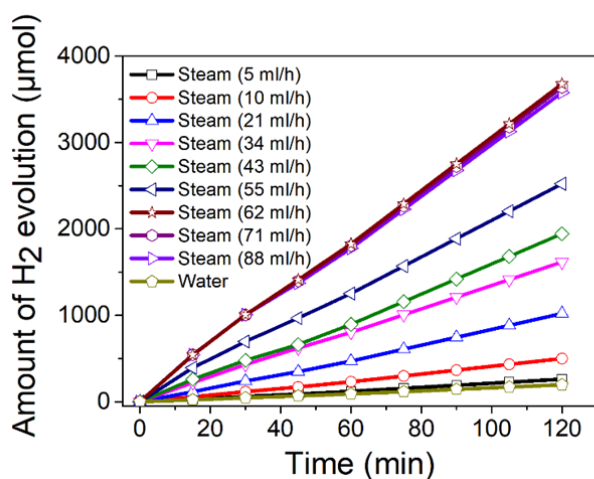


Figure R2 (*i.e.*, Supplementary Figure 17 in the original version). Time-dependent photocatalytic hydrogen gas production profiles from the liquid water and water steam with different flow rates. The photocatalyst is CoO NPs.

2) In the catalysis process, H₂O₂ was produced from water, and these H₂O₂ is able to be accumulated on the surface of the wood. Will these accumulated H₂O₂ have any

effect on the durability of the device when it was maintained under illumination for a long period (e.g. 8 h for 5 days)?

Response: We thank the reviewer for the insightful comment. According to the reviewer's suggestion, we have carried out the durability measurement on the wood/CoO system for an extended period (8 h for 5 days). As shown in Figure R3, the amount of H₂ evolution increases linearly along with the measurement time (8 h/day for 5 days). On day 5, the photocatalytic hydrogen evolution performance maintains about 90 % of that in day 1, indicating the good durability of the wood/CoO device. The accumulated H₂O₂ seems to have little effect on hydrogen production stability.

In the revised version, Figure R3 is added as a new Figure 2d; and the related discussion has been added in the main text.

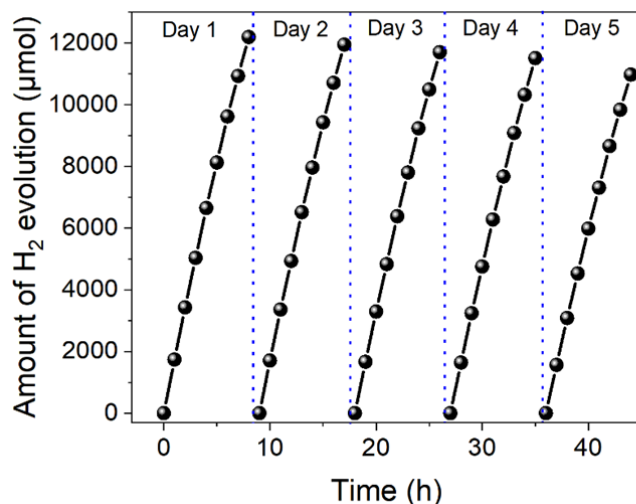


Figure R3. Time-dependent photocatalytic gas production profiles from the wood/CoO for a long-period measurement (8 h for 5 days).

3) The catalyst was spin coated on the surface of the wood, so will the catalyst be very easy to detach from the substrate? This might cause the loss of the catalyst, resulting

in the contamination of bulk water.

Response: Thanks very much for the valuable comments. In our work, the catalyst was spin-coated on the surface of the wood, which was dried in an oven at 45 °C for 2 h to help improve the catalyst adhesion to the wood channels. We compared the SEM images and EDS element mapping of CoO NPs attached to the wood microchannels before and after the photocatalytic reaction, as shown in Figure R4 and R5. No apparent changes could be observed. Besides, the UV-Vis spectrum of the water in the wood/CoO system after the photocatalytic reaction has been measured as shown in Figure R6. There are no CoO characteristic peaks in the absorption spectrum, indicating that CoO was not detached from the wood to contaminate the water system.

In the revised version, Figure R6 of the absorption spectrum from the water in the wood/CoO system is added as Supplementary Figure 13 in the Supporting Information; and the related discussion has been added in the main text.

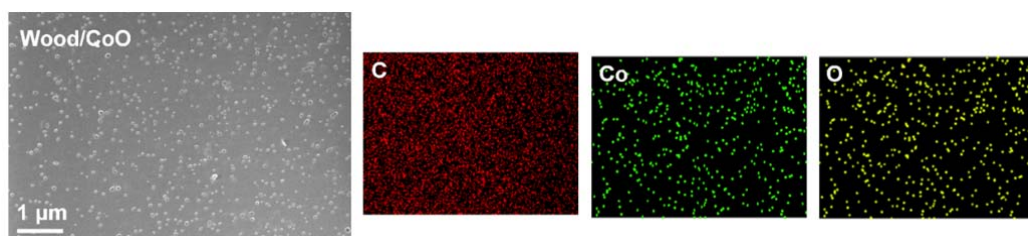


Figure R4 (*i.e.*, Supplementary Figure 10 in the original version). SEM images and EDS element mapping of CoO NPs attached to the walls of the wood microchannels before photocatalytic reaction.

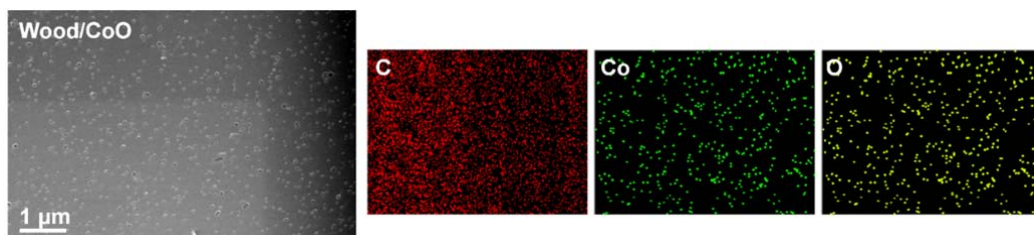


Figure R5 (*i.e.*, Supplementary Figure 11 in the original version). SEM images and

EDS element mapping of CoO attached to the walls of the wood microchannels after the photocatalytic reaction.

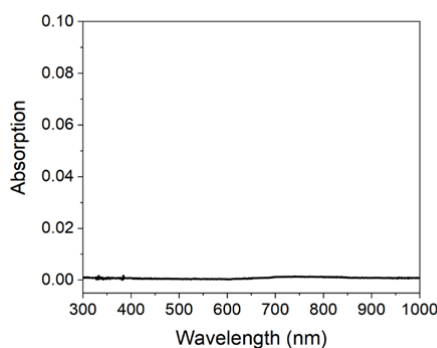


Figure R6. The absorption spectrum from the water in the wood/CoO system.

4) The catalytic reactivity of the photocatalytic reaction is related to the solar intensity and reaction temperature. Therefore, the solar intensity might not be in a linear relation with the hydrogen production rate. Their relationship need to be further explored.

Response: Thanks for the great suggestion. Accordingly, solar intensity (100, 200, and 300 mW/cm²) on the photocatalytic reaction of the wood/CoO system has been investigated. As shown in Figure R7, the rate of hydrogen evolution grows with solar intensity, but not linearly related to the hydrogen production rate as predicted by the reviewer. This is mainly because of the rise of temperature on the wood/CoO surface caused by the increase in solar intensity. As shown in Figure R8, the temperature of the wood/CoO surface is increased to 324, 342, and 357 K when the solar power of 100, 200, and 300 mW/cm² is applied, respectively. In addition, we have already studied the temperature effect on the rate of hydrogen evolution under the same solar intensity illumination (100 mW/cm²). As shown in Figure R9, the temperature can exponentially improve hydrogen production. Thus, the relationship between the rate

of hydrogen evolution and solar intensity could be nonlinear.

In the revised version, the rate of H₂ evolution against solar intensity in the wood/CoO system (Figure R7) and infrared radiation thermal images (Figure R8) are added as the new Figure 2c and Supplementary Figure 9 in the Supporting Information, respectively. The related discussion has been added to the main text.

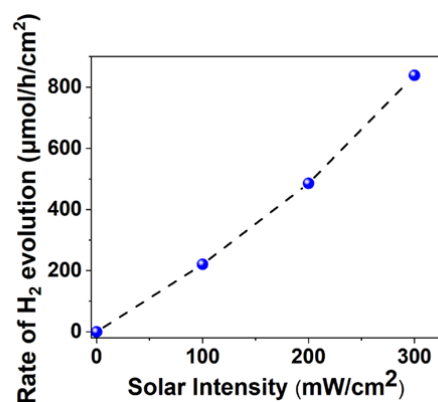


Figure R7. Rate of H₂ evolution versus solar intensity in the wood/CoO system.

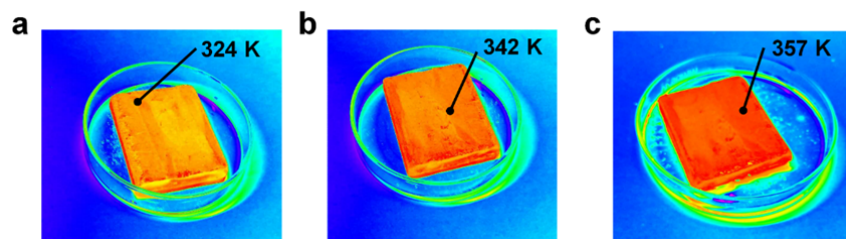


Figure R8. Infrared radiation thermal images of the wood/CoO system under light illumination with different solar intensity. **a** 100 mW/cm², **b** 200 mW/cm², **c** 300 mW/cm².

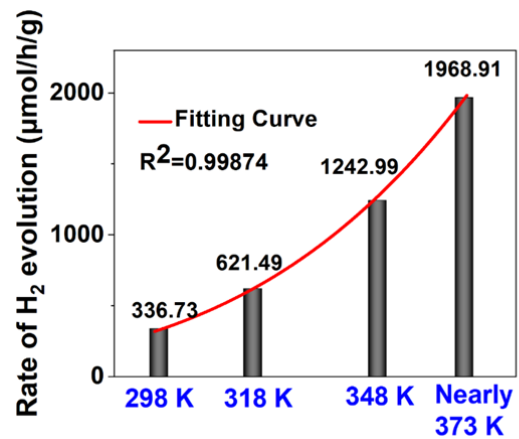


Figure R9 (*i.e.*, Figure 4a in the original version). The photocatalytic hydrogen evolution rate with the CoO NPs versus the reaction temperature in the triphase reaction system.

Reviewer #2:

The manuscript describes an experimental study on the photothermal-photocatalytic properties of wood/CoO composite materials. The authors extensively discuss the hydrogen evolution rates of the prepared material, the influence of the state of water (liquid vs. gas) and try to reveal the universality of the approach by utilization of various light-absorbing materials. As such applying photothermal transpiration to produce (solar) steam without additional energy input is quite interesting but the reported data raise some questions. Particularly, the absence of stoichiometric amounts of oxygen (or hydrogen peroxide) are indicative for either a sacrificial reagent (e.g. the wood) participating in the reaction or the general instability of the CoO and particularly the CuS/MoS₂ catalyst where it is even highlighted that NO O₂/H₂O₂ has been detected; so what is oxidized in this case? Therefore, claiming overall water splitting is not justified and any comparison with other systems performing overall water splitting is meaningless.

Response: Thanks for the comments. The typical photocatalysts we selected in this work mainly produce H₂, and only the half-reaction for H₂ production has been involved. There are three reaction paths for the photo-induced holes in the photocatalytic hydrogen production reaction, including (1) reaction with sacrificial reagents, (2) by-products formation such as H₂O₂, and (3) reaction with the catalyst surface. In the wood/CoO case, the main reaction path for the photo-induced holes is H₂O₂ production, which has been confirmed by detecting the quantity of H₂O₂ after the photocatalytic reaction. As shown in Figure RR1, the H to O ratio would satisfy

2:1 with the consideration of the H_2O_2 amount. This is convincing evidence to prove the wood without the sacrificial agent effect. In the CuS/MoS_2 case, H_2O_2 is not detectable. Some previous studies demonstrated the surface reaction for metal sulfides during the photocatalytic reaction process (J. Mater. Chem. A, 2015, 3, 13913; Sol. Energy, 2018, 171, 106; Catal. Commun., 2014, 44, 62). Similarly, the photo-induced holes could react with S ions from the CuS/MoS_2 catalysts in the current work as shown based on the XPS results (Figure RR2).

Considering the oxygen generation issue, we only compared photocatalytic hydrogen production performance with other systems rather than the overall water splitting. Therefore, the comparison is reasonably fair.

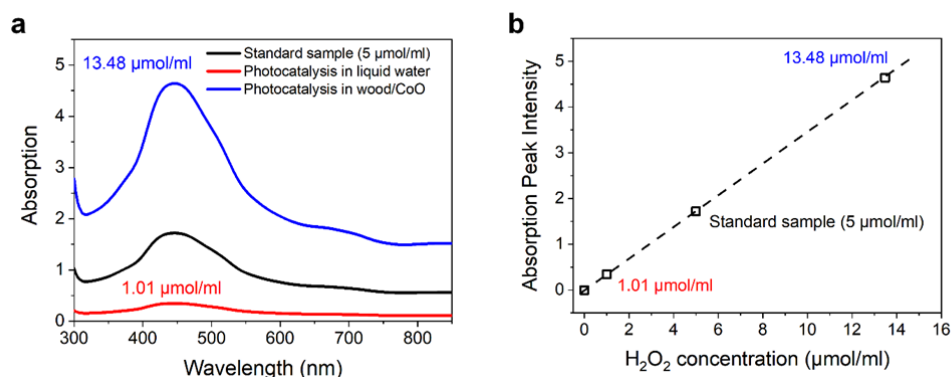


Figure RR1 (*i.e.*, Supplementary Figure 16 in the original version). The H_2O_2 concentration determination from absorption spectra. (a) the absorption spectra from different H_2O_2 concentrations and (b) the linear fitting between the intensity of absorption peak and H_2O_2 concentration.

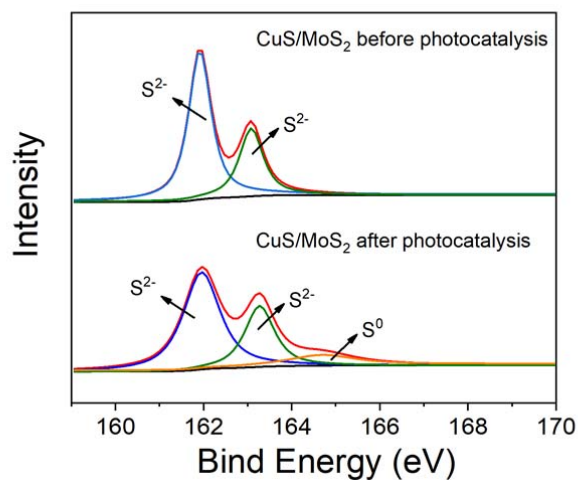


Figure RR2 The high-resolution XPS of element S for CuS/MoS₂ before and after photocatalytic reaction.

Additionally, it is widely expected in photocatalysis that a comparison photocatalysts based on production rates should be avoided. Instead QY or AQY should be reported. It is also advised to report rates here on a per cm² basis rather than a per g basis given the significant dimensions of the wood used.

Response: Thanks for the comments. It is understood that QY or AQY, determined by the photoelectric properties of a photocatalyst, should be provided if a new catalyst is developed. However, in the current work, we focused on the interface regulation between water molecules and photocatalysts rather than the photocatalysts themselves. The photocatalysts we selected to demonstrate our proof-of-concept are all typical photocatalysts and have been intensively reported in the literature. In the wood/photocatalyst system, only the catalytic environment is varied from liquid water to water steam, and nothing has changed regarding the photocatalysts. Therefore, it is not necessary to measure the QY or AQY here.

We thank the reviewer for the excellent advice on the unit, i.e., the production rate per cm^2 . In the revised version, we modified the production rate quantitative unit in Figures 2 (a)-(c).

Generally, it is advise to thoroughly reconsider the wording, i.e. record-high hydrogen production.

Response: We agree with the reviewer and modified “record-high hydrogen production” to be “impressive hydrogen production”.

Additional minor details are:

- The authors suggest stability of the system based on (HR)TEM data. However, comparing Fig S5 and S14 significant agglomeration is evident and the surface of the particles seems to be less ordered. Given that the wood substrate is essential a thorough characterization is required. This should be included and stability of the system clarified.

Response: Thanks very much for the valuable comments. First, the catalyst CoO NPs were spin-coated to the wood matrix, and it is challenging to realize the uniform dispersion of CoO NPs. However, the current preparation method is straightforward, low-cost, and greatly advantageous for practical applications. In the future, some templated methods could be considered for ordered NPs loading. Regarding the thorough characterization of the wood/CoO, we further performed the TEM and EDS element mapping to investigate the whole wood/CoO system. As shown in Figures RR3 and RR4, the CoO NPs are still attached to the wood channels after the

photocatalytic reaction, exhibiting the good adhesion stability of photocatalysts. In addition, the UV-Vis spectrum of the bulk water in the wood/CoO system after the photocatalytic reaction has been measured as shown in Figure RR5. There is no CoO characteristic peak in the absorption spectrum, exhibiting that the catalyst CoO is still attached to the wood. Moreover, the reflection spectra of the wood/CoO system have also been measured before and after the photocatalysis process, as shown in Figure RR6. There is little difference in the reflection spectra of the wood/CoO system before and after the photocatalysis process, exhibiting the excellent stability of the wood/CoO system.

In the revised version, the TEM images (Figure RR3 and RR4), reflection spectra (Figure RR6) of the wood/CoO system before and after the photocatalytic reaction, and the absorption spectrum of the bulk water in the wood/CoO system after the photocatalytic reaction (Figure RR5) are added as the new Figures 2e and 2f in the main text and as Supplementary Figures 12 and 13 in the Supporting Information. Related discussions have been added to the main text.

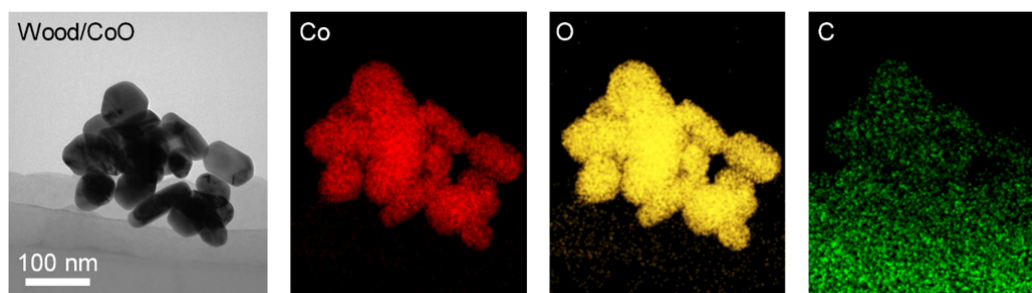


Figure RR3. TEM image and EDS element mapping of CoO NPs attached to the walls of the wood microchannels before photocatalytic reaction.

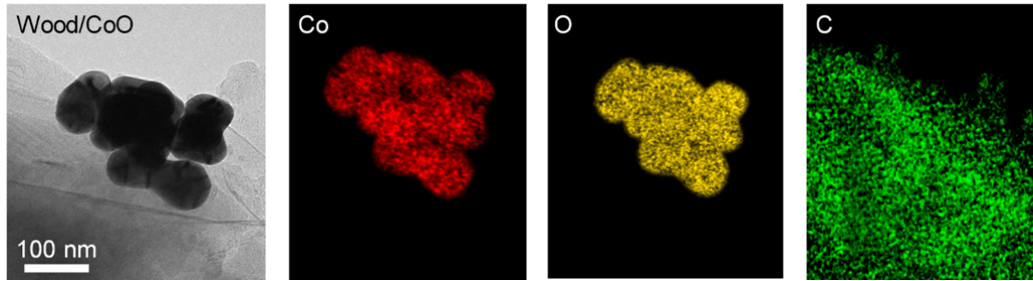


Figure RR4. TEM image and EDS element mapping of CoO attached to the walls of the wood microchannels after the photocatalytic reaction.

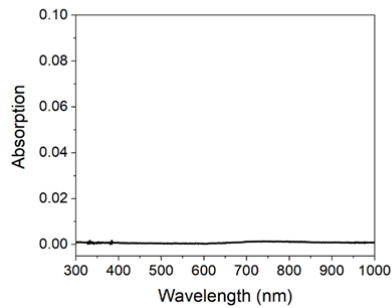


Figure RR5. The absorption spectrum from bulk water in the wood/CoO system after the photocatalytic reaction.

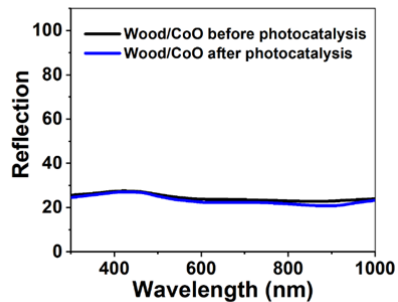


Figure RR6. The reflection spectra of the wood/CoO system before and after the photocatalysis process.

- It is not clear whether only steam is reacting to H_2 or also liquid water is involved in the reaction. Given that hydrogen peroxide is detected in the liquid phase it might be the later. The author should provide a concise picture illustration the processes occurring.

Response: Thanks very much for the valuable comments. In the current work, only

steam participated in producing H_2 . Liquid water was not involved in the reaction because the photocatalysts in the wood system did not have contact with liquid water. This claim is evidenced by the Raman spectrum to confirm the CoO NPs distributed approximately 2 mm along the walls of the wood microchannels. As shown in Figure RR7, when the wood/CoO system floats on the surface of the water, the immersion depth of the wood in the water is about 2 mm, indicating that the photocatalysts are not directly soaked in the liquid phase water.

It is unfortunate that “hydrogen peroxide is detected in the liquid water” generated confusion. The reality is H_2O_2 was produced from the photocatalytic reaction with steam in the wood/CoO system. To analyze the H_2O_2 quantity with absorption spectra (Figure RR1), we had to wash the wood with liquid water, into which H_2O_2 was fully dissolved.

To eliminate the misunderstanding, we redraw a schematic of the photocatalytic reaction process, as shown in Figure RR8. Under light illumination, the adhered photocatalysts become covered with water steam produced by the photothermal transpiration in the wood interior. Simultaneously, the photo-induced electrons generated in the photocatalysts participate in the hydrogen evolution reaction at the photocatalytic active sites, and the photo-induced holes participate in the H_2O_2 generation. The new schematic of the photocatalytic reaction process (Figure RR8) is added as Figure 1a, and the related discussion has been added in the revised manuscript.

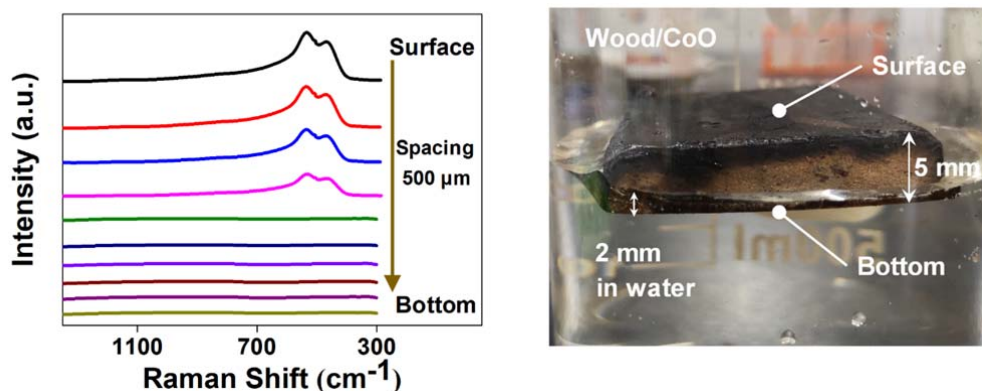


Figure RR7 (*i.e.*, Figure 1 in the original version). (left) Raman spectra taken at different depths along the cross-section of the wood/CoO microchannels with an interval of 500 μm . (right) the photo of the wood/CoO system floating on the surface of water.

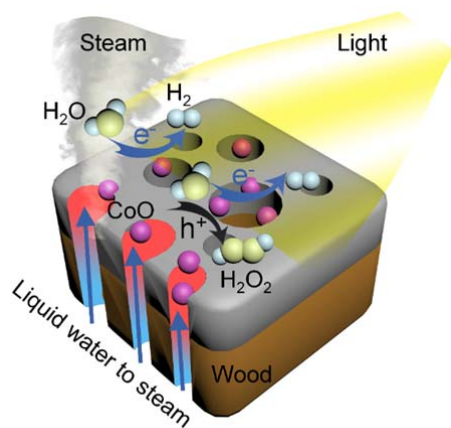


Figure RR8. Schematic of the photocatalytic reaction process of the wood/CoO system.

- The dependence of CoO loading should be addressed. Is this an optimized configuration?

Response: Thanks very much for the valuable suggestion. We investigated the effect of CoO NPs mass loading in the wood/CoO system on the photocatalytic hydrogen gas production rates (see Figure RR9) via varying the CoO concentration during the

spin-coating process. Photocatalytic hydrogen production rates with different catalyst mass loadings are analyzed within a constant surface area of wood (area: 7.85 cm^2). An optimized mass loading of about 38 mg/cm^2 CoO NPs has been identified based on the experimental results.

In the revised version, Figure RR9 is added as the new Figure 2a in the main text; and the related discussion has been added in the revised manuscript.

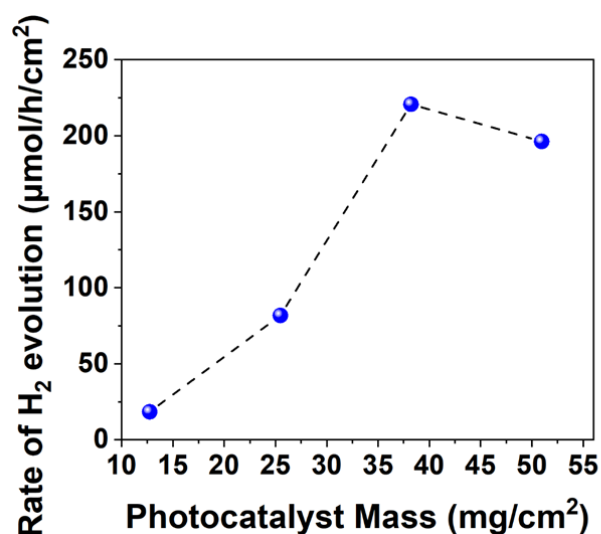


Figure RR9. Mass loading-dependent photocatalytic hydrogen gas production rates for the wood/CoO system (area: 7.85 cm^2).

- The authors report that a solar simulator is used placed 7 cm above the sample. However, it is not clear whether 100 mW/cm^2 are obtained at the sample surface.

Response: Thanks for raising the question. In fact, the light intensity of 100 mW/cm^2 was calibrated at the distance of 7 cm from the solar simulator through the optical power meter (CEL-NP2000), as shown in Figure RR10.

In the revised version, the photograph of the light intensity measurement is added as Supplementary Figure 33 in the supporting information.



Figure RR10. The photograph of the light intensity measurement.

- The authors report thermal images and indicate that only a minor increase in temperature is observed at the surface of the wood/CoO system. The local temperature at the nm scale (size of the CoO particles) however might be much higher. The authors should comment on local vs. global temperature effects.

Response: Thanks very much for the insightful comments. We agree with the reviewer that the local temperature could be significantly different from the global temperature. The local temperature of the nanoscale CoO particles under light illumination can be estimated through the potential, which can be measured using Atomic Force Microscopy (Annu. Rev. Mater. Sci., 1999, 29, 505). According to this reference, there is a correlation between the potential and the temperature. Therefore, we first measured the potential of CoO particles at two different temperatures (the temperature was pre-set), 300 K and 308 K, as shown in Figures RR11 a and b. Then, the potential of CoO particles under 100 mW/cm^2 light illumination was measured, as shown in Figure RR11 c. Based on the relationship between potential and the temperature, the local temperature of CoO particles under 100 mW/cm^2 light

illumination is estimated to be 346 K (Figure RR11 d), which, as expected, is higher than the global temperature (325 K, in Figure RR12) because of the nanoscale effect. It is speculated that a higher local temperature is beneficial to enhance the photocatalytic reaction efficiency.

In the revised version, Figure RR11 is added as Figures 1f and 1g in the main text and Supplementary Figure 7 in the Supporting Information; and the related discussion has been added in the main text. We thank the reviewer for a very useful suggestion.

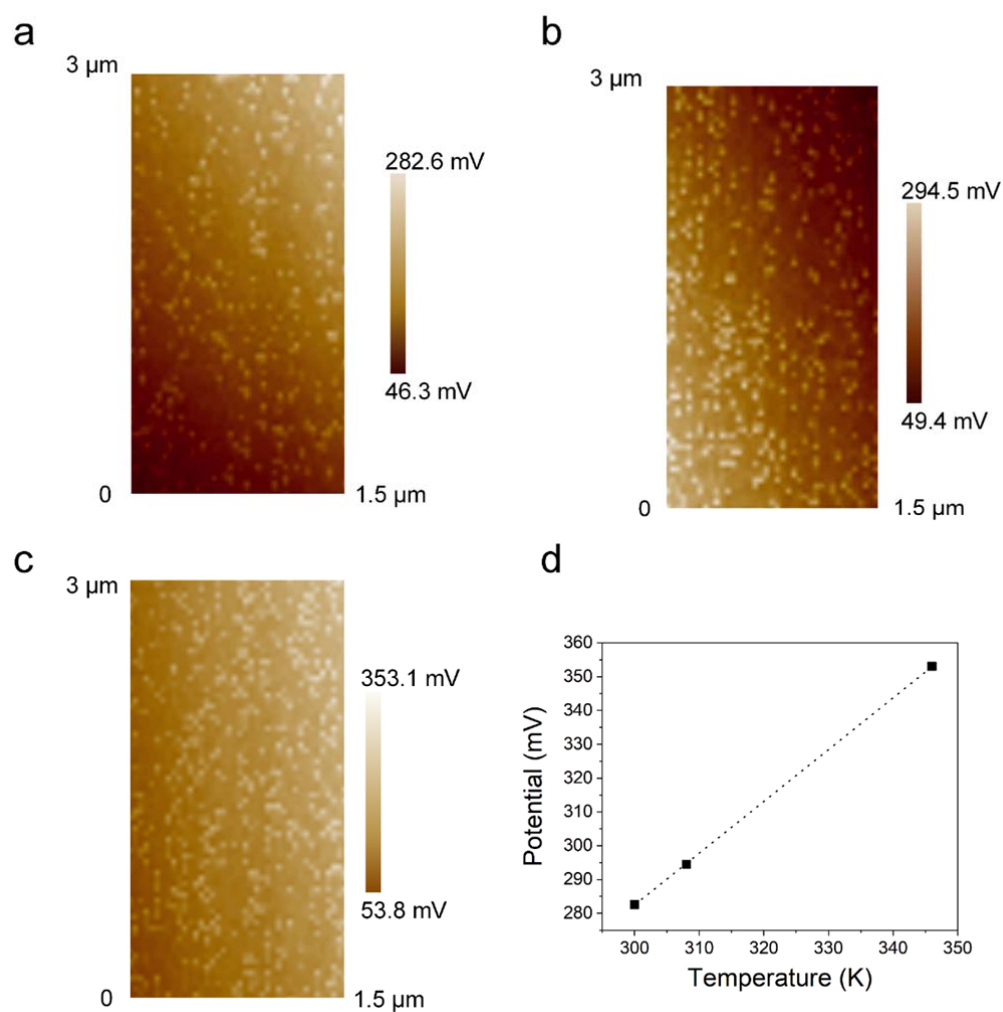


Figure RR11. **a** The potential of wood/CoO at 300 K, **b** the potential of wood/CoO at 308 K, **c** the potential of wood/CoO under 100 mW/cm² light illumination, and **d** the estimated temperature through the potential.

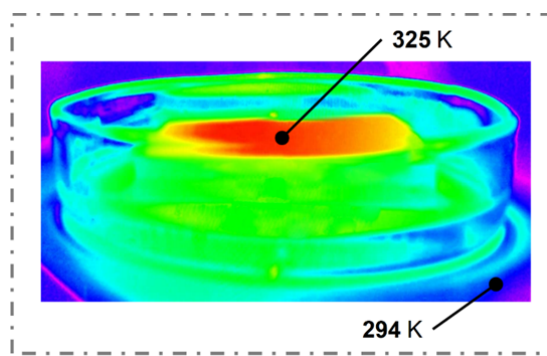


Figure RR12 (*i.e.*, Figure 1e in the original version). Infrared radiation thermal image from the wood/CoO system under light illumination.

- The authors should use appropriate and original literature, *i.e.* techno-economics used to justify the benefits of a PC system are not reported in Ref. 2. Additionally it is questionable whether the techno-economics of a PC system are actually applicable in this case as the reactor design and dimensions are significantly deviating from a true PC system.

Response: Thanks for the comments. We have double checked and confirmed that the “techno-economics used to justify the benefits of a PC system” was expressed in the first paragraph of Ref. 2 though this techno-economic discussion of photocatalysis was originally reported in the literature (Energy Environ. Sci., 2013, 6, 1983). Anyway, to avoid confusion and downplay the techno-economic discussion, we have rephrased the sentence: “There are three main types of solar-driven hydrogen production systems: particulate photocatalysis, photovoltaic-assisted electrolysis (PV-E), and photoelectrochemical cells (PEC)², where the particulate photocatalysis is predicted to be more cost-effective than the other two systems⁴”, in the revision. The original literature (Energy Environ. Sci., 2013, 6, 1983) was also cited as ref. 4.

Reviewer #3:

In the present manuscript the authors add a novel twist to the by now well known class of carbon-supported nanoparticle catalysts where, instead of using a well defined carbon material, they use charred wood. While this unquestionably makes the whole setup much less well defined than even mesoporous carbon supports, they were able to show that this setup leads to tremendously improved hydrogen production rates in photo-catalytic water splitting. The effect of the charred wood thereby seems to be the fact that it produces water vapour near the catalytic nanoparticles which then favourably influences the overall reaction rates. Given that humanity is still on the hunt for adequate alternative energy production methods and storage media, the discovery of a novel photocatalyst for water splitting is in principle of utmost importance. All the more so considering the ubiquity of the new support material.

Due to my background in theory I do not think my opinion on the experimental methods used in this work will be necessary. I will, however, comment on the theoretical calculations the authors conducted, which, frankly, are so far below the current state of the art to render the results essentially meaningless. As I will outline in detail below, I do not think that any of the calculations undertaken here are of sufficient predictive quality, which to be honest also would make me somewhat suspicious of the rest of the work.

Response: Thanks very much for the valuable comments. In the revised version, we have tried our best to strengthen the theoretical calculation with more direct evidences and sufficient details. The new results still support our conclusion. The retained results

will be discussed with specific problems the reviewer asked below.

These are the specific problems I found with the manuscript:

1) The structural model. Which slab did the authors use, was it a surface unitcell or a supercell, how many layers did they include? This is really the most basic information and the authors fail to give it.

Response: Thanks very much for the valuable comments. As shown in Figure RRR1, The (111) surface of CoO with rock salt crystal structure was modeled with a 2×2 supercell containing 13 atomic layers, where 5 layers were fixed in the bulk positions. All slab structure included a vacuum of 15 Å. Besides, H and OH groups were also modeled to the CoO (111) surface to comparatively analyze the photocatalytic process.

In the revised version, Figure RRR1 of structure schemes of CoO, CoO-H, and CoO-OH has been added as Supplemental Figure 34 in the Supporting Information; and the details of the CoO model structures have been added in the Theoretical Calculation section of the main text.

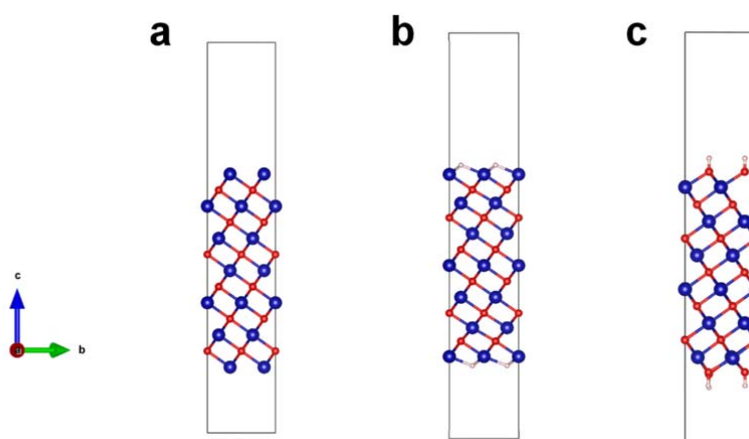


Figure RRR1. The model structure schemes of (a) CoO, (b) CoO-H, and (c)

CoO-OH.

2) I assume, because it is never actually stated, that the authors simulated CoO in its rocksalt structure. In which case the O-terminated (111) facet is actually partially charged, meaning their simulation cell should (if they simulated stoichiometric CoO, also not stated) show a quite sizeable dipole perpendicular to the surface. This is well known and most works compensate for this, yet there is no mention of such a compensation in this work.

Response: Thanks very much for the valuable comments. In our calculation, the dipole compensation was applied to eliminate the field influence from the asymmetric plate system. In other words, the dipole moment correction was considered and added in the calculation optimization process. The antiferromagnetic moment was set up along the (111) direction.

In the revised version, we have added the crystal structure of CoO and the clarification of the dipole compensation in the Theoretical Calculation section.

3) One possibility why the authors did not encounter a surface dipole is because the PBE functional used in this work likely yields a metallic electronic structure for CoO. Not knowing the specifics, I would nevertheless assume that their material has a band gap, otherwise it would not be a photo-catalyst. Again, this is a well known and understood failure of GGA functionals. Yet, with such a broken electronic structure I do not think that the calculated binding energies show anything but a fortuitous overlap with reality.

Response: Thanks very much for the valuable comments. In our work, DFT+U calculations were performed using VASP with PAW pseudopotentials provided in the VASP database and the RPBE-generalized gradient approximation (GGA) exchange-correlation functional. A U value of 4.1 eV was applied to the Co d-states. Based on the methods, the band structures of CoO (including CoO, CoO-H, and CoO-OH) have been obtained. As shown in Figure RRR2, the CoO (including CoO, CoO-H, and CoO-OH) show semiconductor band structures rather than the metallic electronic structure. The bandgap is about 2.3 eV, which is consistent with the experimental results based on the absorption spectrum of CoO NPs (Supplementary Figure 6).

In the revised version, Figure RRR2 of band structures of different CoO models, including CoO, CoO-H, and CoO-OH, have been added as Supplemental Figure 35 in the Supporting Information; and the details of the calculation method have been supplemented in the Theoretical Calculation section.

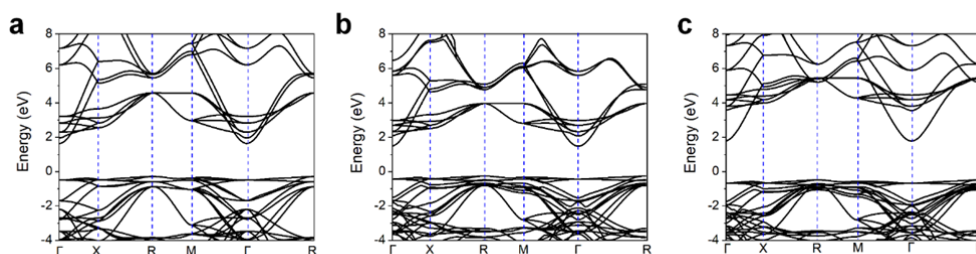


Figure RRR2. The band structures of CoO (a), CoO-H (b), and CoO-OH (c).

4) Why did the authors simulate the de-protonated CoO facet? What pH are they aiming for? Most studies nowadays at least try to determine the protonation state of their surface (which btw. could be one way to avoid the aforementioned surface dipole)

beforehand.

Response: Thanks very much for the valuable comments. In our work, the surface dipole was considered and corrected in the calculation optimization process (see the answers to Question 2). And the de-protonated CoO facet was simulated to analyze the hydrogen adsorption on the pure CoO surface here (Experimentally, the pH value of the reactant water is approximately equal to 7). Besides, the CoO facet was constructed with the H and OH groups to simulate the different CoO status in the water molecules environment. It was possible that some groups (i.e., H and OH) could be attached to the surface of CoO. The surface groups (i.e., H and OH) could also realize the surface dipole compensation.

Here, the pure CoO structure, CoO with H groups, and CoO with OH groups could simulate the different situations in the neutral, acid, alkaline environment. Moreover, the pH effect was also considered implicitly through the formula $\Delta G = \Delta E + \Delta E_{ZPE} - T\Delta S + \Delta G_{pH} + \Delta G_{sol}$. ΔE is the adsorption energy, ΔE_{ZPE} is the difference in zero point energy, T is the temperature, and ΔS is the difference in entropy between the adsorbed species and free species in the gas phase. At different pH values, $\Delta G_{pH} = 0.059 \times \text{pH}$; and ΔG_{sol} represents the correction terms for solvent effect (0 eV for H* and 0.5 eV for OH*) (J. Mater. Chem. A, 2019, 7, 3648). The Gibbs free energies of hydrogen evolution reaction from the three different CoO structures were calculated to analyze the thermodynamics in the photocatalytic process. As shown in the Figures RRR3-RRR5, in the different pH environment, both temperature and water phase status significantly affect the water molecule adsorption

process to reduce the barriers, which demonstrate advantageous to the photocatalytic hydrogen evolution reaction.

In the revised version, Figure RRR3 of the Gibbs free energies of the hydrogen evolution reaction from the pure CoO structure is added as Figures 4b and 4c, and Figures RRR4 and RRR5 of the Gibbs free energies of the hydrogen evolution reaction from the CoO-H and CoO-OH structures are added as Supplemental Figures 21 and 22 in the supporting information. And the related discussion is added in the main text.

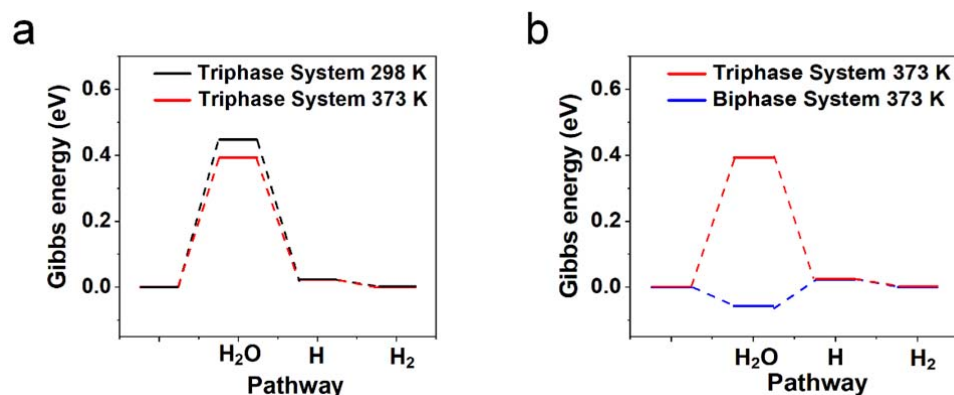


Figure RRR3. **a** Gibbs energy of a photocatalytic reaction on the pure CoO surface at different temperatures in the triphase system. **b** Gibbs energy of a photocatalytic reaction on the pure CoO surface in the triphase system in comparison with the biphasic system at 373 K.

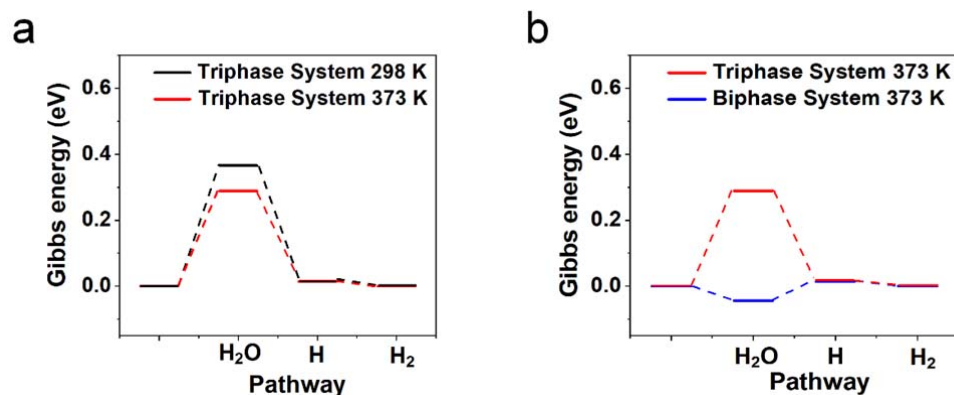


Figure RRR4. **a** Gibbs energy of a photocatalytic reaction over the CoO-H structure at different temperatures in the triphase system. **b** Gibbs energy of a photocatalytic

reaction over the CoO-H structure in the triphase system in comparison with the biphase system at 373 K.

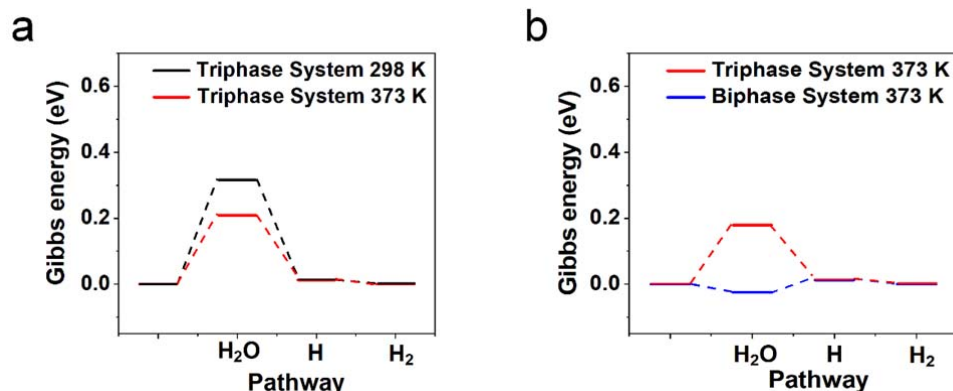


Figure RRR5. **a** Gibbs energy of a photocatalytic reaction over the CoO-OH structure at different temperatures in the triphase system structure. **b** Gibbs energy of a photocatalytic reaction over the CoO-OH structure in the triphase system in comparison with the biphase system at 373 K..

5) It is completely unclear to me how the authors are supposed to have calculated the Gibbs free energies in the bi- and tri-phasic systems. Did they actually include solvent effects? If so, how? As it is, the way Figure 3c came to be is entirely unclear to me.

Response: Thanks very much for the valuable comments. In our work, the Gibbs free energies in both bi- and tri-phasic systems were calculated based on the formula $\Delta G = \Delta E + \Delta E_{ZPE} - T\Delta S + \Delta G_{pH} + \Delta G_{sol}$. ΔE is the adsorption energy. ΔE_{ZPE} is the difference in zero-point energy. T is the temperature, and ΔS is the difference in entropy between the adsorbed species and free species in the gas phase. The differences of Gibbs free energies in the bi- and tri-phasic systems are the temperature (373 K and 298 K, respectively) and the entropy change ΔS . The entropy change ΔS correction in the vapor water and liquid water was obtained from the Handbook of Chemistry and Physics. The entropy S is 0.367 kJ/(kg•K) at 298 K under the standard pressure, while at 373 K the entropy S is 1.303 kJ/(kg•K) when the water is

liquid (the value is used for Gibbs free energies calculation in tri-phasic systems at 373 K) and 7.361 kJ/(kg•K) when the water is in the gas phase (the value is used for Gibbs free energies calculation in bi-phasic systems at 373 K).

The solvent effect was considered through the CoO surface facet modification with the H and OH groups to simulate the CoO status in the water molecule's environment. Moreover, the solvent effect was also considered implicitly through the formula $\Delta G = \Delta E + \Delta E_{ZPE} - T\Delta S + \Delta G_{pH} + \Delta G_{sol}$. At different pH values, $\Delta G_{pH} = 0.059 \times pH$; and ΔG_{sol} represents the correction term for solvent effect (0 eV for H* and 0.5 eV for OH*) (J. Mater. Chem. A, 2019, 7, 3648). As shown in Figures RRR3-RRR5, it is easily noticed that the adsorption process of water molecules in the bi-phasic system is improved, compared to that in the tri-phasic system, which favors the enhancement on the photocatalytic hydrogen evolution reaction.

In the revised version, the details on the calculation of Gibbs free energies in the bi- and tri-phasic systems and solvent effect are supplemented in the Theoretical Calculation section.

6) In order to determine some of the Gibbs free energies, the authors apply a technique now known as the computational hydrogen electrode, by J. Norskov and J. Rossmeisl (eq. 5 in the present work). While this is indeed state of the art, I find it mildly suspicious that the authors neglect to cite any of the original works here.

Response: Thanks for the comment and sorry for our carelessness. It was not intended to omit the originality. The original works from J. Norskov and J. Rossmeisl

(Chem. Phys., 2005, 319, 178; J. Phys. Chem. B 2004, 108, 17886) have been cited as Refs. 69 and 70 in the revised manuscript.

7) Finally, not a point directly related to the first-principles calculations, but with eq. 1 the authors calculate the effective free energy barrier of their reaction, yet fail to use it for anything than mildly extrapolating towards higher temperatures. Why is this barrier not discussed or at least compared to other setups? I am sure the kinetic barriers on pristine CoO can by now be found in the literature.

Response: Thanks very much for the valuable comments. Before we discuss the barrier, please allow me to discuss why we used Eq. 1. The primary purpose of Eq. 1 in the current work is to calculate the H₂ evolution rate at 373 K by fitting the experimental results between H₂ evolution reaction rate V and reaction temperature T (from 298 K to close to 373 K) in the triphase reaction system. According to Eq. 1, the H₂ evolution rate at 373 K is estimated to be 2236.76 μmol/h/g. However, it is much lower than the experimentally obtained H₂ evolution rate (6200.42 μmol/h/g, see Fig. 3d) in the biphasic reaction system at the same temperature of 373 K, indicating that in addition to reaction temperature, the state of water plays a crucial role in enhancing the hydrogen evolution of the biphasic reaction system.

Regarding the barrier, the activation energy for the hydrogen production over the CoO NPs was deduced to 23.023 kJ/mol after we used Eq. 1 to fit the experimental results between H₂ evolution reaction rate V and reaction temperature T. The activation energy of CoO NPs is lower than that of Co-CoO_x-graphene with ammonia

borane (62.3 kJ/mol) (Chem. Asian J. 2020, 15, 1) and CoO-NRs with NaBH₄ (27.4 kJ/mol) (Appl. Catal. A-Gen. 2020, 589, 117303). The activation energy is a key indicator to reflect whether photocatalytic hydrogen evolution reaction becomes easier. The smaller the activation energy is, the easier the hydrogen production process will become. Therefore, the hydrogen production process is easily conducted for the current CoO NPs.

In the revised version, the related discussion about the Eq. 1 and reaction activation energy are supplemented in the main text.

REVIEWER COMMENTS

Reviewer #1 (Remarks to the Author):

The author addressed all my technical comments in the revised manuscript to my satisfaction. With the added experimental data and analysis the authors also improved the level of scientific advancement presented in this work. The consideration of publishing this revised manuscript is thus recommended.

Reviewer #2 (Remarks to the Author):

This is the second time that I am reviewing this work. The authors significantly improved the article based on the comments of the reviewers. Still not all comments have been sufficiently addressed and as such there are still some concerns that require revisions before the article might be acceptable for publication in Nat. Commun.

- In the abstract the authors now mention impressive hydrogen production rate up to 85604 $\mu\text{mol/g/h}$. First I still suggest to be concise throughout the manuscript and use (if at all) rates normalized per area exposed as any scaling of the technology will be done using sheet like structures. Second the system providing these H₂ rates is NOT stable and as such I consider this to be inappropriate for the abstract. Given that most of the article is focused on the somewhat stable CoO/wood system I would advise to highlight this finding in the abstract
- It is noted that the hydrogen production decreases not only from day 1 to day 5 but also the accumulated amount of hydrogen throughout 8h of operation is decreasing. This should be discussed in the manuscript and it is important to emphasize that all rates are initial and not average rates obtained during 8h of illumination. Also it is still not clear what is causing the overall decrease to 90% of H₂ production already after 5 cycles. This rate of deactivation is still sufficient to consider the material unstable.
- It is still mandatory to use AQY/QY especially for the comparison performed in Fig. 5e. Given that photocatalyst dispersion is affected by anchoring to the wood substrate and in turn light scattering, particle etc is different to normal liquid phase systems using suspended particles. The variation in reactor and process design renders the comparison only meaningful if AQY/QY are used.
- The authors argue that H₂O₂ production as shown in Figure RR1 (plus evolved oxygen shown elsewhere) satisfy stoichiometric production of H₂ and "O"-species. Based on the numbers provided this is not understandable and additional details/calculations should be provided to unambiguously show stoichiometric production
- The provided stability analysis is still superficial: Particle detachment should be studied appropriate sensitive tools like elemental analysis rather than UV-VIS.

Reviewer #3 (Remarks to the Author):

The authors addressed most of my points. I am now convinced that most of their methodology is quite sound. There are only two approximations left which are still not discussed by the authors and they both concern the solvent corrections.

1) The values taken for the solvent corrections were not actually computed in reference 71. Instead reference 71 (in the supporting information, from which the two sentences in the lines 441 and 442 were copied verbatim) cites another work (Acs Catal, 2015, 5, 6658-6664) which did indeed perform calculations to estimate the free energy correction of adsorbates due to solvent. Yet, these corrections were calculated for metal particles on graphene (the original work) and then used for extended platinum in 71. Considering that the structuring of water on graphene, platinum and on oxides can be radically different (see for example any work by A. Gross and co-workers), I would think that the

direct usage of these values quite a large approximation (already in reference 71), which at least needs to be discussed.

2) In calculating the overall Gibbs free energies for the bi- and triphasic systems the authors only vary the direct entropic contribution neglecting that the solvation correction most definitely depends on the state of the solvent. This is quite easy to see if one considers that liquid water's dielectric permittivity is a lot larger than that of water vapor. The omission of this effect might explain the large differences in the free energy profiles of the two systems.

Both those points are quite strong simplifications which could have been easily avoided had the authors used e.g. an implicit solvation model in their VASP calculations. I suggest that the authors either discuss their approximations properly or avoid them altogether. As it is, I still cannot support the manuscript's publication.

Point-by-point Response to the Reviewers' Comments

Reviewer #1 (Remarks to the Author):

The author addressed all my technical comments in the revised manuscript to my satisfaction. With the added experimental data and analysis the authors also improved the level of scientific advancement presented in this work. The consideration of publishing this revised manuscript is thus recommended.

Response: We thank the reviewer for the encouragement.

Reviewer #2 (Remarks to the Author):

This is the second time that I am reviewing this work. The authors significantly improved the article based on the comments of the reviewers. Still not all comments have been sufficiently addressed and as such there are still some concerns that require revisions before the article might be acceptable for publication in Nat. Commun.

Response: We thank the reviewer for reviewing and providing insightful comments to improve the manuscript's quality.

- In the abstract the authors now mention impressive hydrogen production rate up to 85604 $\mu\text{mol/g/h}$. First I still suggest to be concise throughout the manuscript and use (if at all) rates normalized per area exposed as any scaling of the technology will be done using sheet like structures. Second the system providing these H_2 rates is NOT stable and as such I consider this to be inappropriate for the abstract. Given that most of the article is focused on the somewhat stable CoO/wood system I would advise to highlight this finding in the abstract.

Response: We thank the reviewer very much for the valuable suggestions. The hydrogen production rate unit " $\mu\text{mol h}^{-1} \text{g}^{-1}$ " has been replaced by " $\mu\text{mol h}^{-1} \text{cm}^{-2}$ " throughout the manuscript. For example, 85604 $\mu\text{mol h}^{-1} \text{g}^{-1}$ has been converted to be 3271.49 $\mu\text{mol h}^{-1} \text{cm}^{-2}$. We have also revised the abstract to specify the wood/CoO system as below: "As a result, an impressive hydrogen production rate up to 220.74 $\mu\text{mol h}^{-1} \text{cm}^{-2}$ in the particulate photocatalytic systems has been achieved based on the wood/CoO system, demonstrating that the photothermal-photocatalytic biphasic

system is cost-effective and greatly advantageous for practical applications.”

- It is noted that the hydrogen production decreases not only from day 1 to day 5 but also the accumulated amount of hydrogen throughout 8h of operation is decreasing. This should be discussed in the manuscript and it is important to emphasize that all rates are initial and not average rates obtained during 8h of illumination. Also it is still not clear what is causing the overall decrease to 90% of H₂ production already after 5 cycles. This rate of deactivation is still sufficient to consider the material unstable.

Response: We thank the reviewer for the useful comments. The description of hydrogen production has been revised as “On day 1, the initial hydrogen production rate in 1 h reaction is 221.56 $\mu\text{mol h}^{-1} \text{cm}^{-2}$, and the average hydrogen production rate during 8 h reaction is 194.14 $\mu\text{mol h}^{-1} \text{cm}^{-2}$. On day 5, the average hydrogen production rate during 8 h reaction is 174.73 $\mu\text{mol h}^{-1} \text{cm}^{-2}$. Thus, after 5 days (40 hours) test, the photocatalytic stability can be significantly improved through the wood/catalysts system compared to that in the previous work, which only holds 1 h of reaction²⁶.”

Regarding the CoO stability issue, many researchers attributed the CoO deactivation to the corroded or oxidized surfaces of CoO during the photocatalytic reaction. For example, Bao et al. found that the CoO becomes seriously deactivated after only 1 hour of reaction due to the corroded or oxidized surfaces of CoO, demonstrating that the CoO is relatively unstable (Nature Nanotechnology, 2014, 9, 69). However, in our current work, the photocatalytic stability of the CoO has been significantly improved. Even in 40 hours of reaction, the amount of H₂ production

maintains 90 % for the designed wood/CoO system. The possible reason for this is that the wood/CoO system with water steam provides a mild reaction condition relative to the triphase system with liquid water (J. Electrochem. Soc., 2020, 167, 066502; ACS Appl. Mater. Interfaces, 2019, 11, 41267)

This related discussion has been added on pages 7 and 8 of the main text in the revised version.

- It is still mandatory to use AQY/QY especially for the comparison performed in Fig. 5e. Given that photocatalyst dispersion is affected by anchoring to the wood substrate and in turn light scattering, particle etc is different to normal liquid phase systems using suspended particles. The variation in reactor and process design renders the comparison only meaningful if AQY/QY are used.

Response: Thanks very much for the valuable suggestion. The apparent quantum yield

(AQY) is calculated based on the formula below (Energy Environ. Sci. 2017, 10, 1643):

$$AQY = \frac{2 \cdot n \cdot N_A}{(E \cdot A \cdot T \cdot \lambda) / (h \cdot C)} \times 100\% \quad (1)$$

where, n is the H₂ yield, N_A is the Avogadro number, E is light intensity, A is the irradiation area, T is the time, λ is the wavelength, h is the Planks constant, C is the speed of light. The comparison of AQY with literature in different particulate photocatalytic systems has been modified, as shown in Figure R1. And the measured data is listed in Table R1. The wood/photocatalyst biphasic photothermal-photocatalytic systems show the dominant AQY in each catalyst field.

In the revised version, Figure 5e has been modified for the catalytic performance comparison based on AQY in the main text. And Table R1 is added as Supplementary Table 2 in the Supporting Information.

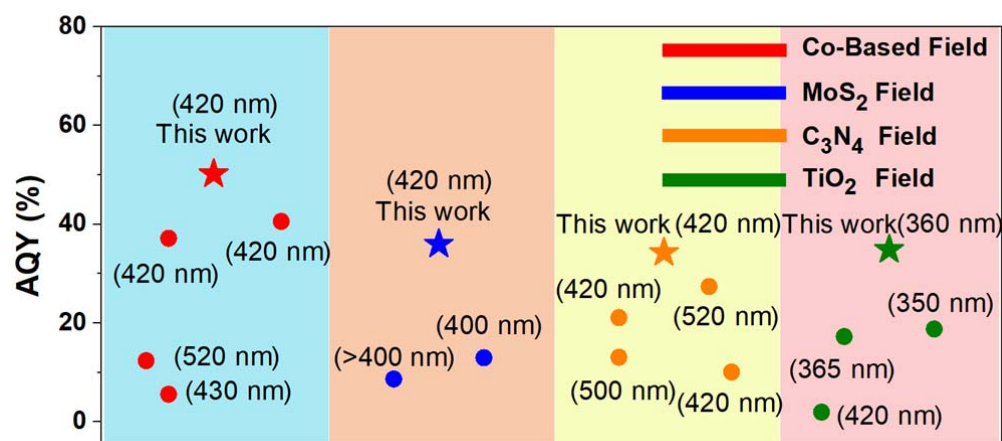


Figure R1. Comparison of the AQY with literature in different particulate photocatalytic systems of TiO₂, C₃N₄, MoS₂, and Co-based photocatalysts. The numbers are the wavelength information. Note: the maximum AQY data in literature and measurement results are presented for comparison.

Table R1. The measurement information for AQY calculation, including catalysts, wavelength, light intensity, and H₂ yield.

Catalysts	Wavelength (nm)/ Light intensity (mW cm ⁻²)	H ₂ yield (μmol)/ AQY (%)
Wood/CoO	380/13.82	255.01/41.1
Wood/CoO	420/16.32	405.85/50.1
Wood/CoO	500/12.32	325.77/44.8
Wood/MoS ₂	380/13.77	195.87/31.7
Wood/MoS ₂	420/16.59	295.25/35.9
Wood/MoS ₂	500/11.97	223.16/31.5
Wood/C ₃ N ₄	380/13.63	122.67/20.0
Wood/C ₃ N ₄	420/16.12	273.49/34.2
Wood/C ₃ N ₄	500/12.43	175.35/23.9
Wood/TiO ₂	360/13.54	193.74/33.6
Wood/TiO ₂	380/16.87	90.24/11.9

- The authors argue that H₂O₂ production as shown in Figure RR1 (plus evolved oxygen shown elsewhere) satisfy stoichiometric production of H₂ and “O”-species. Based on the numbers provided this is not understandable and additional details/calculations should be provided to unambiguously show stoichiometric production.

Response: We thank the reviewer for the comments. The calculation details are provided below.

Regarding the triphase system (Figure R2, i.e., Supplementary Figure 15 in the original version), after the 120-minute test, the amount of H₂ evolution is about 196.98 μmol, and the amount of O₂ evolution is approximately 48.04 μmol. After the reaction, the H₂O₂ concentration is 1.01 μmol ml⁻¹ in 100 ml reaction solvent (note that the H₂O₂ concentration is calculated through the absorption spectrum, Figure R3, i.e., Supplementary Figure 17 in the original version). Thus the amount of H₂O₂ is 101 μmol. H₂O₂ converts to O₂ following the reaction equation below:



Combining the amount of directly produced O₂ (48.04 μmol) and the amount of indirectly converted O₂ from H₂O₂ (50.50 μmol), the total amount of O₂ is 98.54 μmol. Thus, the production ratio of H₂ and O₂ is 196.68:98.54 (i.e., 1.99:1).

For the wood/CoO system (Figure R4, i.e., Supplementary Figure 16 in the original version), the amount of H₂ evolution is about 3677.55 μmol, and the amount of O₂ evolution is about 1121.21 μmol after 120 min test. The H₂O₂ concentration is

13.48 $\mu\text{mol ml}^{-1}$ in 100 ml reaction solvent after the catalytic reaction (Figure R3, i.e., Supplementary Figure 17 in the original version). Thus, the amount of H_2O_2 is 1348 μmol . Combining the amount of directly produced O_2 (1121.21 μmol) and the amount of indirectly converted O_2 from H_2O_2 (674 μmol), the total amount of O_2 is 1795.21 μmol . Considering the above calculation, the production ratio of H_2 and O_2 is 3677.55:1795.21 (i.e., 2.04:1).

In the revised version, this calculation details about stoichiometric production have been added in the Supporting Information.

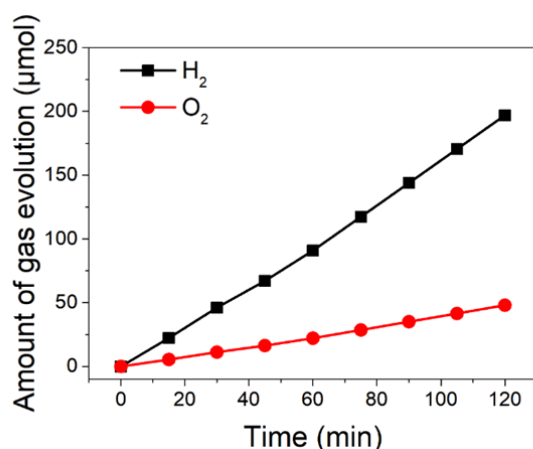


Figure R2 (i.e., Supplementary Figure 15 in the original version). Time-dependent photocatalytic gas production profiles from the triphase system. The photocatalyst is CoO NPs.

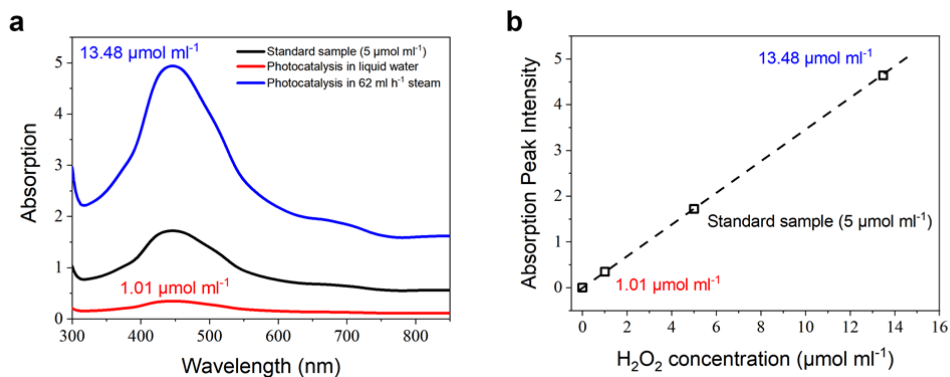


Figure R3 (i.e., Supplementary Figure 17 in the original version). The H_2O_2 concentration determination from absorption spectra. (a) the absorption spectra from

different H_2O_2 concentration, and (b) the linear fitting between absorption peak and H_2O_2 concentration. The calculation details of H_2O_2 concentration: The $5 \mu\text{mol ml}^{-1}$ H_2O_2 was used as the standard sample to react with copper (II) sulfate solution and 2,9-dimethyl-1,10-phenanthroline (DMP) solution, and the obtained absorption spectrum was used as the baseline. Due to the linear relationship between absorption peak and H_2O_2 concentration, the H_2O_2 concentration in the solution after the photocatalytic reaction could be calculated based on the above absorption spectra. After the photocatalytic reaction, the concentration of H_2O_2 measured is about 1.01 and $13.48 \mu\text{mol ml}^{-1}$ for the triphase reaction system and wood/CoO systems, respectively.

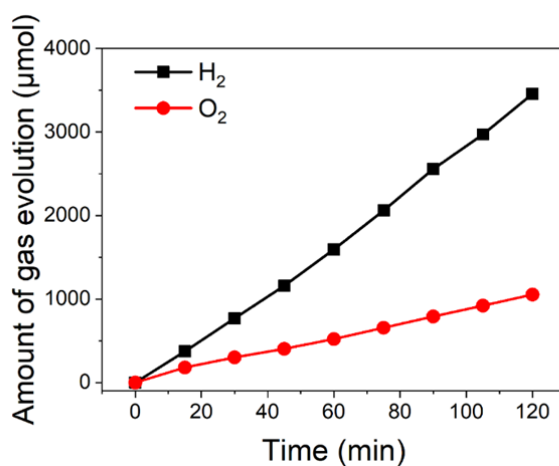


Figure R4 (i.e., Supplementary Figure 16 in the original version). Time-dependent photocatalytic gas production profiles from the wood/CoO.

- The provided stability analysis is still superficial: Particle detachment should be studied appropriate sensitive tools like elemental analysis rather than UV-VIS.

Response: We thank the reviewer for the valuable suggestion. The photocatalytic particle stability has been further studied through X-ray photoelectron spectroscopy (XPS) and inductively coupled plasma emission spectrometer (ICP). As shown in Figure R5, the XPS spectra of the wood/CoO system maintain relatively unchanged after the catalytic reaction. The high-resolution element spectra of elemental C, Co,

and O have also been displayed in Figure R5, exhibiting little change before and after the catalytic reaction. Besides, the ICP of the bulk water in the wood/CoO system after the photocatalytic reaction has also been measured, and a trace amount of element Co in the bulk water is observed, indicating the excellent particle stability of the wood/CoO system (Table R2).

In the revised version, the XPS and ICP results have been added as Supplementary Figure 13 and Supplementary Table 1 in the Supporting Information. The related discussion has been added on page 8 of the main text.

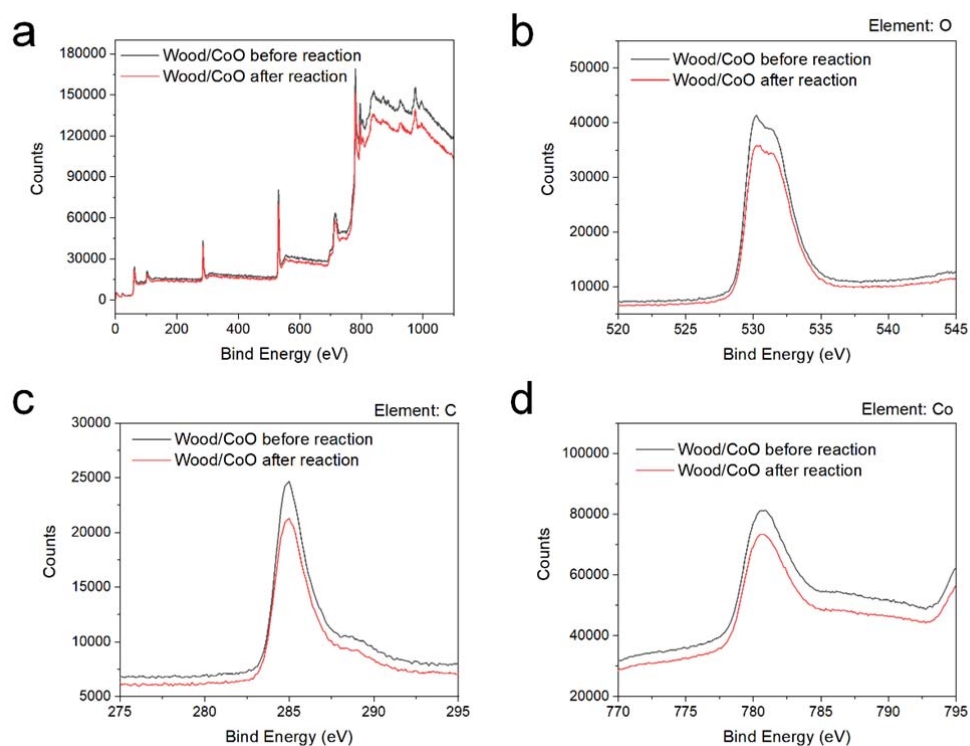


Figure R5. The XPS spectra of the wood/CoO system before and after photocatalysis process. **a** XPS full spectrum of the wood/CoO system before/after the reaction, **b** high-resolution XPS of element O, **c** element C, and **d** element Co for the wood/CoO system.

Table R2. The element Co concentration in the bulk water from the wood/CoO

system after the photocatalytic reaction based on the ICP measurement. Three samples were tested.

	Sample 1	Sample 2	Sample 3
Element Co Concentration ($\mu\text{g ml}^{-1}$)	0.0102	0.0123	0.0088

Reviewer #3 (Remarks to the Author):

The authors addressed most of my points. I am now convinced that most of their methodology is quite sound. There are only two approximations left which are still not discussed by the authors and they both concern the solvent corrections.

1) The values taken for the solvent corrections were not actually computed in reference 71. Instead reference 71 (in the supporting information, from which the two sentences in the lines 441 and 442 were copied verbatim) cites another work (Acs Catal, 2015, 5, 6658-6664) which did indeed perform calculations to estimate the free energy correction of adsorbates due to solvent. Yet, these corrections were calculated for metal particles on graphene (the original work) and then used for extended platinum in 71. Considering that the structuring of water on graphene, platinum and on oxides can be radically different (see for example any work by A. Gross and co-workers), I would think that the direct usage of these values quite a large approximation (already in reference 71), which at least needs to be discussed.

2) In calculating the overall Gibbs free energies for the bi- and triphasic systems the authors only vary the direct entropic contribution neglecting that the solvation

correction most definitely depends on the state of the solvent. This is quite easy to see if one considers that liquid water's dielectric permittivity is a lot larger than that of water vapor. The omission of this effect might explain the large differences in the free energy profiles of the two systems.

Both those points are quite strong simplifications which could have been easily avoided had the authors used e.g. an implicit solvation model in their VASP calculations. I suggest that the authors either discuss their approximations properly or avoid them altogether. As it is, I still cannot support the manuscript's publication.

Response: We thank the reviewer very much for the valuable suggestion. The two questions are both related to solvent corrections and can be answered together. We agreed with the reviewer and have chosen the implicit solvation model to avoid the simplification problem of solvent corrections because the implicit solvation model considers the effect of water's dielectric permittivity. The implicit solvent models are calculated using the VASPsol (J. Chem. Phys. 2014, 140, 084106; J. Chem. Phys. 2019, 151, 234101), where the dielectric constants of liquid water and gas water are indexed to be 81 and 1, respectively from the Handbook of Chemistry and Physics. As a result, the Gibbs energy of a photocatalytic reaction can be calculated to better explain the bi- and triphasic systems' differences, as shown in Figure R6. Compared to that in the tri-phasic system, it is easily noticed that the water molecule adsorption process in the bi-phasic system is much more favorable to the photocatalytic hydrogen evolution reaction. It is concluded that the calculation results with the implicit solvation model still support our findings.

The details on the calculation of implicit solvent models are supplemented in the Theoretical Calculation section in the revised version. And the related discussion is added in the main text.

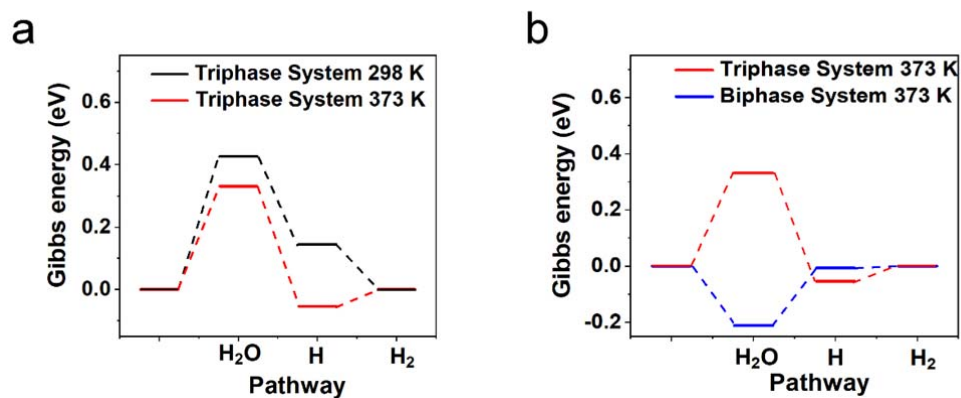


Figure R6. **a** Gibbs energy of a photocatalytic reaction on the pure CoO surface at different temperatures in the triphase system. **b** Gibbs energy comparison of a photocatalytic reaction on the pure CoO surface at 373 K in bi- and triphasic systems.

REVIEWERS' COMMENTS

Reviewer #2 (Remarks to the Author):

The author addressed all my comments in the revised manuscript. The revised manuscript is thus recommended for publication.

Reviewer #3 (Remarks to the Author):

The authors addressed my last point. I am now convinced that their theoretical results are based on a sound state of the art methodological approach. I have found no further reasons preventing the publication of this manuscript in Nature Communications.

Point-by-point response to reviewers' comments

Reviewer #2 (Remarks to the Author):

The author addressed all my comments in the revised manuscript. The revised manuscript is thus recommended for publication.

Response: Thanks very much for the comments.

Reviewer #3 (Remarks to the Author):

The authors addressed my last point. I am now convinced that their theoretical results are based on a sound state of the art methodological approach. I have found no further reasons preventing the publication of this manuscript in Nature Communications.

Response: Thanks very much for the comments.